Static Surface Mode Expansion for the Electromagnetic Scattering From Penetrable Objects

Carlo Forestiere, *Member, IEEE*, Giovanni Gravina, Giovanni Miano, Guglielmo Rubinacci, and Antonello Tamburrino, *Senior Member, IEEE*

***Abstract*— We introduce longitudinal and transverse static surface modes and use them to solve the scattering problem from penetrable objects with arbitrary shapes. The longitudinal static modes are the eigenmodes, with zero surface-curl, of the electrostatic integral operator that determines the tangential component of the electric field, as a function of the surface charge density. The transverse static modes are the eigenmodes, with zero surface-divergence, of the magnetostatic integral operator that determines the tangential component of the vector potential, as a function of the surface current density. These static modes are solely determined by the object's shape, thus, the same static basis can be used regardless of the operating frequency or material properties. We expand the unknown surface currents of the Poggio-Miller-Chang-Harrington-Wu–Tsai (PMCHWT) equation in terms of the static modes and solve it using Galerkin-projections. The static modes expansion allows for the regularization of the integral operators and also leads to a significant reduction in the number of unknowns compared to a discretization based on sub-domain basis functions. As a consequence, the CPU-time required for the numerical solution of the scattering problem from arrays of identical particles is significantly reduced by employing an expansion in terms of static modes of the isolated particle.**

***Index Terms*— Computational electromagnetics, dielectric resonators, eigenvalues and eigenfunctions, electromagnetic scattering, integral equations, plasmonics, resonance, resonators.**

I. Introduction

THE analysis of the electromagnetic scattering from a collection of mutually coupled objects is of great importance for many applications, spanning from antenna arrays [1] to metasurfaces [2] and metalens [3]. In this context, the use of integral formulations is appealing, since the unknowns are defined only within the objects' volume or, if the objects are spatially piecewise homogeneous, on their boundary and internal interfaces. Additionally, these formulations naturally satisfy the radiation condition at infinity. Nevertheless, the corresponding discrete problem is characterized by dense matrices, and their inversion is usually associated with high computational burden, even when acceleration techniques such as fast multipole algorithms are implemented [4].

Accurate and efficient solutions of integral formulations heavily depend on the choice of basis functions. Two main categories of basis functions can be distinguished: *sub-domain* functions, which are nonzero only over a portion of the object, or *entire-domain* functions, which extend over the entire domain of the object. While sub-domain functions may have wider applicability and are more suitable for objects with irregular shapes and sharp corners, entire-domain functions are very appealing when multiple scattering problems are considered, where the electromagnetic system under investigation is a collection of mutually-coupled objects [5], [6], [7].

Representative examples of sub-domain functions include the Rao-Wilton–Glisson functions [8], loop/star functions [9], [10], [11], [12], loop/tree functions [13], Trintinalia–Ling functions [14], Buffa–Christiansen functions [15], higher order vector basis functions of Nédélec type [16], etc.

On the other hand, examples of entire-domain basis functions include the tangential vector spherical wave functions [17], [18] and the tangential vector spheroidal wave functions [19]. Specifically, the former functions have been exploited to carry out a systematic analysis of integral operators of potential theory [17] and to investigate stability and preconditioning of multiple traces formulations for electromagnetics [18].

Analytical entire-domain bases may be generated in coordinate systems where the Helmholtz equation is separable. A different strategy to generate entire domain basis functions even in irregular domains is to introduce a convenient auxiliary eigenvalue problem. This is done for instance with characteristic modes [20], [21], [22], [23], (see [5], [6] for arrays of perfectly conductive particles and [24] for perfectly conductive metasurfaces). The characteristic modes do not depend on the particular excitation conditions, and they are effective in the numerical solution of scattering problems from collections of objects of a given material at a fixed operating frequency. Nevertheless, characteristic modes do depend on the frequency, and their interesting properties are lost if they are used as basis at a frequency different from the one at which they are computed. Thus, they may not be the best choice when the scattering problem has to be solved at multiple frequencies since they have to be recalculated at each frequency.

In this article, we introduce a different set of entire domain basis functions that we call "static" surface current modes. These modes are the union of two sets: longitudinal and

Manuscript received 11 November 2022; revised 28 April 2023; accepted 10 May 2023. Date of publication 16 June 2023; date of current version 4 August 2023. *(Corresponding author: Carlo Forestiere.)*

Carlo Forestiere, Giovanni Miano, and Guglielmo Rubinacci are with the Department of Electrical Engineering and Information Technology, Università degli Studi di Napoli Federico II, 80125 Naples, Italy (e-mail: carlo.forestiere@unina.it).

Giovanni Gravina is with the Department of Electrical Engineering and Information Technology, Università degli Studi di Napoli Federico II, 80125 Naples, Italy, and also with the 10th Aircraft Maintenance Department, Italian Air Force, Galatina, 73013 Lecce, Italy.

Antonello Tamburrino is with the Dipartimento di Ingegneria Elettrica e dell'Informazione "M. Scarano," Università degli Studi di Cassino e del Lazio Meridionale, 03043 Cassino, Italy.

Color versions of one or more figures in this article are available at https://doi.org/10.1109/TAP.2023.3285356.

Digital Object Identifier 10.1109/TAP.2023.3285356

transverse modes, exhibiting vanishing surface curl and surface divergence, respectively. We assemble these two sets by solving two *auxiliary* frequency-independent eigenvalue problems, involving Hermitian and positive-definite surface integral operators, having the *static* Green's function as a kernel.

The representation of the surface current in terms of longitudinal (irrotational) and transverse (solenoidal) static modes implements a Helmholtz decomposition on a surface (e.g., [25]). In the context of electromagnetic problems, the idea of splitting a field into its irrotational and solenoidal components has been pioneered by Nédélec [26] and has emerged as a very powerful tool for theoretical analysis of integral formulations [17], [18], [27].

The static surface current modes are the low-frequency limit of the resonance modes of surfaces of finite conductivity [28]. Their volume counterparts have been presented in [29] and [30] and in [31] where they have been already used to expand the electromagnetic field [32], [33], [34], [35].

The static modes can be also considered as "high level expansion functions", belonging to the same categories of the functions introduced in [36], [37], [38], and [39], which are typically used in the solution of integral equations in electrically large structure to reduce the number of unknowns. They are not bound to the conventional discretization limit of $\lambda/20$, to which the local basis function discretization is constrained. The proposed basis shares similarities with the one introduced by Vecchi et al. [40], [41] and is used in a hybrid spectral–spatial method for the analysis of printed antennas.

We expand the unknown surface currents of the Poggio-Miller–Chang–Harrington–Wu–Tsai (PMCHWT) equation in terms of the static surface modes and solve it using the Galerkin-projection scheme. The PMCHWT equation [21], [42], [43], [44] is a surface integral formulation of Maxwell's equation, belonging to the class of single-trace methods [45]. We demonstrate the following advantages of employing the static modes: 1) regularization of the scattering integral operator; 2) "compression" of the matrix equation, which is associated with a significant reduction of the number of unknowns compared to sub-domain basis functions while maintaining solution accuracy; and 3) reduction of the CPU-time required for the solution of multiple scattering problems. The static mode basis can be also used in the context of multiple-trace methods, which were recently proposed for electromagnetic scattering from composite objects [18], [46], [47], [48], [49], [50].

The article is organized as follows: in Section II we introduce the static basis; in Section III we recall the PMCHWT formulation and we show that the static mode expansion regularizes the involved operator and that a proper rescaling of the unknowns makes this formulation immune from the low-frequency breakdown. In Section IV, we validate the introduced method in two resonant scattering problems, namely the scattering from a metal particle and high-permittivity particle in the visible/near-infrared spectral range. Lastly, we demonstrate the application of this method to solve a multiple-scattering problem. In Section VI we draw the conclusion.

II. Static Surface Current Modes

We denote with Ω a bounded 3-D domain, whose boundary $\partial\Omega$ is "sufficiently regular" [51]; $\hat{\mathbf{n}}$ is the normal to $\partial\Omega$ pointing outward. A sufficiently smooth vector field $\mathbf{j}$ defined on a regular surface $\partial\Omega$ can be resolved into the sum of two components [25], [26], [27], [52]: an irrotational and nonsolenoidal vector field $\mathbf{j}^{\parallel}$ and a solenoidal and rotational (nonzero curl) vector field $\mathbf{j}^{\perp}$. The vector fields $\mathbf{j}^{\parallel}$ and $\mathbf{j}^{\perp}$ are orthogonal according to the scalar product

$$\langle \mathbf{C}, \mathbf{D} \rangle = \int_{\partial\Omega} \mathbf{C}^*(\mathbf{r}) \cdot \mathbf{D}(\mathbf{r}) dS. \tag{1}$$

In the following, we introduce a basis for each of the two components.

A. Longitudinal Static Modes

The longitudinal static surface current modes (called *longitudinal static modes* in the following for brevity) are nontrivial solutions to the eigenvalue problem:

$$\boldsymbol{\mathcal{T}}_0^{\parallel}\left\{\mathbf{j}_k^{\parallel}\right\}(\mathbf{r}) = \gamma_k^{\parallel}\, \mathbf{j}_k^{\parallel}, \quad \text{on } \partial\Omega \tag{2}$$

where

$$\boldsymbol{\mathcal{T}}_0^{\parallel}\{\mathbf{w}\}(\mathbf{r}) = \hat{\mathbf{n}} \times \hat{\mathbf{n}} \times \nabla \oint_{\partial\Omega} g_0(\mathbf{r}-\mathbf{r}') \nabla_S' \cdot \mathbf{w}(\mathbf{r}') dS' \tag{3}$$

$\nabla_S\cdot$ denotes the surface divergence, and g_0 is the homogeneous space static Green's function

$$g_0(\mathbf{r}-\mathbf{r}') = \frac{1}{4\pi} \frac{1}{|\mathbf{r}-\mathbf{r}'|}. \tag{4}$$

Apart from a multiplicative factor, the integral operator (3) determines the tangential component of the static electric field generated by a surface charge density distribution. Its spectrum has the following properties (see [29]).

1) The eigenvalues $\{\gamma_k^{\parallel}\}$ and the modes $\{\mathbf{j}_k^{\parallel}\}$ depend on the shape of the object, but are independent of the object material, and of the frequency of operation.
2) The eigenvalues are real and positive.
3) The modes are orthonormal with respect to the scalar product (1).

For a spherical surface of unit radius, the eigenvalues have the analytical expression

$$\gamma_n^{\parallel} = \frac{n(n+1)}{(2n+1)}, \quad n = 1, 2, 3, \ldots \tag{5}$$

In order to provide the expression of the corresponding modes, we introduce a spherical reference system. The spherical coordinates of the point with position vector $\mathbf{r}$ are (r, θ, ϕ) (with $0 \le r < \infty$, $0 \le \theta < \pi$ and $0 \le \phi < 2\pi$). The basis for the 3-D vector space is the set $(\hat{\mathbf{r}}, \hat{\boldsymbol{\theta}}, \hat{\boldsymbol{\phi}})$, where $\hat{\mathbf{r}}$ is the radial unit vector, $\hat{\boldsymbol{\theta}}$ is the polar unit vector, and $\hat{\boldsymbol{\phi}}$ is the azimuthal unit vector. The $2n+1$ modes corresponding to the degenerate eigenvalue $\gamma_n^{\parallel}$ are the vector spherical harmonics $\mathbf{W}_n^m(\theta, \phi)$ [17], [18] where m is an integer such that $-n \le m \le n$

$$\mathbf{j}_{mn}^{\parallel} = \mathbf{W}_n^m = \hat{\mathbf{r}} \times \mathbf{X}_n^m = \frac{1}{\sqrt{n(n+1)}} \nabla Y_n^m. \tag{6}$$

The spherical harmonic $Y_n^m(\theta,\phi)$ of degree n and order m is given by

$$Y_n^m(\theta,\phi) = C_{mn} P_n^{|m|}(\cos\theta) e^{im\phi} \tag{7}$$

where $P_n^m(\cos\theta)$ is the associated Legendre polynomial of degree n and order m, and C_{mn} is a normalization coefficient. The spherical harmonics are orthogonal. We normalize them in such a way that

$$\int_{\partial\Omega} \left|Y_n^m(\theta,\phi)\right|^2 dS = 1. \tag{8}$$

The normalization coefficient C_{mn} is equal to (e.g., [17])

$$C_{mn} = \sqrt{\frac{2n+1}{4\pi}\frac{(n-|m|)!}{(n+|m|)!}}. \tag{9}$$

The degree n also determines the multipolar order of the vector spherical harmonics (e.g., $n = 1$ for a dipole, $n = 2$ for a quadrupole, etc.,). Thus, (5) shows that longitudinal modes associated with larger eigenvalues $\gamma_n^{\|}$ are characterized by higher multipolar order.

B. Transverse Static Modes

The transverse static surface current modes (called *transverse static modes* in the following for brevity) are nontrivial solutions to the eigenvalue problem:

$$\boldsymbol{\mathcal{T}}_0^{\perp}\{\mathbf{j}_k^{\perp}\}(\mathbf{r}) = \gamma_k^{\perp}\mathbf{j}_k^{\perp}, \quad \text{on } \partial\Omega \tag{10}$$

with

$$\boldsymbol{\mathcal{T}}_0^{\perp}\{\mathbf{w}\}(\mathbf{r}) = -\hat{\mathbf{n}}\times\hat{\mathbf{n}}\times\oint_{\partial\Omega} g_0(\mathbf{r}-\mathbf{r}')\mathbf{w}(\mathbf{r}')dS'. \tag{11}$$

Apart from a multiplicative factor, the integral operator (11) determines the static vector potential generated by a surface current distribution. Its spectrum has the following properties, that can be derived using the standard methods of eigenvalue problems, analogously to [31] and [53].

1) The eigenvalues $\{\gamma_k^{\perp}\}$ and the modes $\{\mathbf{j}_k^{\perp}\}$ depend on the shape of the object, but are independent of the object material and of the frequency of operation.
2) The eigenvalues are real and positive.
3) The modes $\{\mathbf{j}_k^{\perp}\}$ are orthonormal with respect to the scalar product (1).

For a spherical surface of unit radius, the eigenvalues have the analytical expression

$$\gamma_n^{\perp} = \frac{1}{(2n+1)}, \quad n = 1,2,3,\ldots \tag{12}$$

The $2n+1$ modes corresponding to the degenerate eigenvalue $\gamma_n^{\perp}$ are the vector spherical harmonics $\mathbf{X}_n^m(\theta,\phi)$ [17], [18] where m is an integer such that $-n \le m \le n$

$$\mathbf{j}_{mn}^{\perp} = \mathbf{X}_n^m = \frac{1}{\sqrt{n(n+1)}}\nabla Y_n^m \times \mathbf{r}. \tag{13}$$

The degree n also determines the multipolar order of the vector spherical harmonics (e.g., $n = 1$ for a dipole, $n = 2$ for a quadrupole, and so on). Thus, (12) shows that transverse modes associated with smaller eigenvalues $\gamma_n^{\perp}$ are characterized by higher multipolar order.

C. Computation of the Static Modes for Arbitrary Shapes

Let us introduce a surface triangulation of $\partial\Omega$, with N_p vertices, N_t elements, and N_e edges. We represent the static modes in terms of convenient sub-domain basis functions, namely the loop and star functions [12], [54]. Specifically, any longitudinal mode $\mathbf{j}_h^{\|}$ is expanded in terms of (nonsolenoidal) star basis functions $\{\mathbf{j}_p^{\star}\}$ with coefficients $\alpha_{h,p}^{\|}$. Dually, any transverse mode $\mathbf{j}_h^{\perp}$ is expanded in terms of (solenoidal) loop basis functions $\{\mathbf{j}_q^{\circlearrowleft}\}$ with coefficients $\alpha_{h,q}^{\perp}$

$$\mathbf{j}_h^{\|} = \sum_{p=1}^{N_t-1}\alpha_{h,p}^{\|}\,\mathbf{j}_p^{\star}, \quad \mathbf{j}_h^{\perp} = \sum_{q=1}^{N_p-1}\alpha_{h,q}^{\perp}\,\mathbf{j}_q^{\circlearrowleft}. \tag{14}$$

The loop functions are divergence-free, thus they correctly represent the transverse static modes. Instead, the star functions are not curl-free (they are often denoted as quasi-curl [55]), thus they only approximately represent the longitudinal static modes. Both star and loop functions admit a linear representation in terms of Rao–Wilton–Glisson basis functions [8].

For closed surfaces with no handles, the number of linearly independent loop functions is $N_p - 1$, while the number of linearly independent star functions is $N_t - 1$ (see [55] for a discussion on the linear independence of loop and star basis functions). Thus, the numerical auxiliary eigenvalue problem for longitudinal static modes [associated with problem (2)] is

$$\mathrm{T}_0^{\|\star\star}\,\mathbf{J}_h^{\star} = \gamma_h^{\|}\,\mathrm{R}^{\star\star}\,\mathbf{J}_h^{\star} \tag{15}$$

where $(\mathrm{T}_0^{\|\star\star})_{pq} = \langle \mathbf{j}_p^{\star}, \boldsymbol{\mathcal{T}}_0^{\|}\mathbf{j}_q^{\star}\rangle$, $(\mathrm{R}^{\star\star})_{pq} = \langle \mathbf{j}_p^{\star}, \mathbf{j}_q^{\star}\rangle$, and $\mathbf{J}_h^{\star} = [\alpha_{h,1}^{\|}, \alpha_{h,2}^{\|}, \ldots, \alpha_{h,N_t-1}^{\|}]^{\intercal}$. The numerical auxiliary eigenvalue problem for transverse static modes [associated with problem (10)] is

$$\mathrm{T}^{\perp\circlearrowleft\circlearrowleft}\,\mathbf{J}_h^{\circlearrowleft} = \gamma_h^{\perp}\mathrm{R}^{\circlearrowleft\circlearrowleft}\mathbf{J}^{\circlearrowleft} \tag{16}$$

where $(\mathrm{T}^{\perp\circlearrowleft\circlearrowleft})_{pq} = \langle \mathbf{j}_p^{\circlearrowleft}, \boldsymbol{\mathcal{T}}_0^{\perp}\mathbf{j}_q^{\circlearrowleft}\rangle$, $(\mathrm{R}^{\circlearrowleft\circlearrowleft})_{pq} = \langle \mathbf{j}_p^{\circlearrowleft}, \mathbf{j}_q^{\circlearrowleft}\rangle$, and $\mathbf{J}_h^{\circlearrowleft} = [\alpha_{h,1}^{\perp}, \alpha_{h,2}^{\perp}, \ldots, \alpha_{h,N_p-1}^{\perp}]^{\intercal}$.

Since the loop and star functions are not orthogonal [55], the matrices $\mathrm{R}^{\star\star}$ and $\mathrm{R}^{\circlearrowleft\circlearrowleft}$ are not identity matrices, thus (15) and (16) are *generalized* eigenvalue problems. The involved matrices are real, symmetric, and positive definite. Thus, efficient numerical algorithms for the eigenvalue calculation do apply, such as the Cholesky factorization [56]. Moreover, the matrices properties also determine the orthogonality, at the discrete level, of any pair of longitudinal modes, and any pair of transverse modes. The numerical integration of shape functions times the Green's functions or its gradient are evaluated using the techniques introduced by Graglia [57].

III. PMCHWT Surface Integral Equation

A linear, homogeneous, isotropic material occupies the 3-D domain Ω. The material has permittivity $\varepsilon^{+}(\omega)$, permeability $\mu^{+}(\omega)$ and it is surrounded by a background medium with permittivity $\varepsilon^{-}(\omega)$ and permeability $\mu^{-}(\omega)$. The object is illuminated by a time harmonic electromagnetic field $\mathrm{Re}\{\mathbf{E}_{inc}(\mathbf{r})\,e^{i\omega t}\}$. The equivalent electric $\mathbf{j}_e$ and magnetic $\mathbf{j}_m$ surface current densities, defined on $\partial\Omega$, are

solutions of the following surface integral problem formulated by PMCHWT [21], [42], [43]:

$$\mathcal{Z}\,\mathbf{J} = \mathbf{F} \tag{17}$$

where

$$\mathcal{Z} = \begin{pmatrix} \zeta^{-}\boldsymbol{\mathcal{T}}_{-} + \zeta^{+}\boldsymbol{\mathcal{T}}_{+} & \boldsymbol{\mathcal{K}}_{-} + \boldsymbol{\mathcal{K}}_{+} \\ -(\boldsymbol{\mathcal{K}}_{-} + \boldsymbol{\mathcal{K}}_{+}) & \boldsymbol{\mathcal{T}}_{-}/\zeta^{-} + \boldsymbol{\mathcal{T}}_{+}/\zeta^{+} \end{pmatrix} \tag{18}$$

$$\mathbf{J} = \left[\mathbf{j}_e, \mathbf{j}_m\right]^{\mathsf{T}}, \quad \mathbf{F} = [\mathbf{e}_0, \mathbf{h}_0]^{\mathsf{T}}, \tag{19}$$

$$\mathbf{e}_0 = -\hat{\mathbf{n}} \times \hat{\mathbf{n}} \times \mathbf{E}_{inc}\big|_{\partial\Omega}, \quad \mathbf{h}_0 = -\hat{\mathbf{n}} \times \hat{\mathbf{n}} \times \mathbf{H}_{inc}\big|_{\partial\Omega}. \tag{20}$$

The operators $\boldsymbol{\mathcal{K}}_{\pm}$ and $\boldsymbol{\mathcal{T}}_{\pm}$ are the MFIE and EFIE integral operators

$$\boldsymbol{\mathcal{T}}_{\pm}\{\mathbf{w}\}(\mathbf{r}) = jk^{\pm}\hat{\mathbf{n}} \times \hat{\mathbf{n}} \times \int_{\partial\Omega} g^{\pm}(\mathbf{r}-\mathbf{r}')\mathbf{w}(\mathbf{r}')dS' + \frac{1}{jk^{\pm}}\hat{\mathbf{n}} \times \hat{\mathbf{n}} \times \int_{\partial\Omega} \nabla g^{\pm}(\mathbf{r}-\mathbf{r}')\nabla'_S \cdot \mathbf{w}(\mathbf{r}')dS' \tag{21a}$$

$$\boldsymbol{\mathcal{K}}_{\pm}\{\mathbf{w}\}(\mathbf{r}) = \hat{\mathbf{n}} \times \hat{\mathbf{n}} \times \int_{\partial\Omega} \mathbf{w}(\mathbf{r}') \times \nabla' g^{\pm}(\mathbf{r}-\mathbf{r}')dS' \tag{21b}$$

$g^{\pm}$ is the homogeneous space Green's function of the region $\Omega_{\pm}$, i.e.,

$$g^{\pm}(\mathbf{r}-\mathbf{r}') = \frac{e^{-jk^{\pm}|\mathbf{r}-\mathbf{r}'|}}{4\pi|\mathbf{r}-\mathbf{r}'|} \tag{22}$$

$k^{\pm} = \omega\sqrt{\mu^{\pm}\varepsilon^{\pm}}$, and $\zeta^{\pm} = \sqrt{\mu^{\pm}/\varepsilon^{\pm}}$.

A. Galerkin Equations

We aim to solve the PMCHWT (17). To do this, we represent the equivalent electric and magnetic surface currents in terms of the transverse static modes $\{\mathbf{j}_p^{\perp}\}_{p=1,\ldots,N^{\perp}}$ associated with the first $N^{\perp}$ eigenvalues $\gamma_p^{\perp}$ (sorted in descending order), and in terms of the longitudinal static modes $\{\mathbf{j}_q^{\parallel}\}_{q=1,\ldots,N^{\parallel}}$ associated with the first $N^{\parallel}$ eigenvalues $\gamma_q^{\parallel}$ (sorted in ascending order), namely

$$\begin{cases} \mathbf{j}_e(\mathbf{r}) \approx \displaystyle\sum_{p=1}^{N^{\perp}} \alpha_p^{\perp}\mathbf{j}_p^{\perp}(\mathbf{r}) + \sum_{q=1}^{N^{\parallel}} \alpha_q^{\parallel}\mathbf{j}_q^{\parallel}(\mathbf{r}) \\ \mathbf{j}_m(\mathbf{r}) \approx \displaystyle\sum_{p=1}^{N^{\perp}} \beta_p^{\perp}\mathbf{j}_p^{\perp}(\mathbf{r}) + \sum_{q=1}^{N^{\parallel}} \beta_q^{\parallel}\mathbf{j}_q^{\parallel}(\mathbf{r}). \end{cases} \tag{23}$$

The choice of sorting the longitudinal eigenvalues accordingly to an ascending order and the transverse eigenvalues accordingly to a descending order guarantees that low-index eigenvalues are associated with modes of low-order multipoles (dipole, quadrupole, octupole, and so on).

Therefore, we define the unknown block vectors

$$\mathrm{J}_e = \left(\boldsymbol{\alpha}^{\perp}|\boldsymbol{\alpha}^{\parallel}\right)^{\mathsf{T}} \quad \mathrm{J}_m = \left(\boldsymbol{\beta}^{\perp}|\boldsymbol{\beta}^{\parallel}\right)^{\mathsf{T}} \tag{24}$$

with $\boldsymbol{\alpha}^a = [\alpha_1^a, \alpha_2^a, \ldots, \alpha_{\mathrm{N}^a}^a]^{\mathsf{T}}$ and with $\boldsymbol{\beta}^a = [\beta_1^a, \beta_2^a, \ldots, \beta_{\mathrm{N}^a}^a]^{\mathsf{T}}$ and $a = \parallel, \perp$

We find the finite-dimensional approximation of the PMCHWT problem by substituting (23) in (17) and by projecting along the same set of modes, accordingly to a Galerkin projection scheme

$$\mathrm{Z}\,\mathrm{J} = \begin{pmatrix} \mathrm{E}_0 \\ \mathrm{H}_0 \end{pmatrix} \tag{25}$$

where

$$\mathrm{J} = \begin{pmatrix} \mathrm{J}_e \\ \mathrm{J}_m \end{pmatrix} \tag{26}$$

$$\mathrm{Z} = \begin{pmatrix} \zeta^{-}\mathrm{T}_{-} + \zeta^{+}\mathrm{T}_{+} & \mathrm{K}_{-} + \mathrm{K}_{+} \\ -(\mathrm{K}_{-} + \mathrm{K}_{+}) & \mathrm{T}_{-}/\zeta^{-} + \mathrm{T}_{+}/\zeta^{+} \end{pmatrix} \tag{27}$$

$$\mathrm{T}_{\pm} = \left(\begin{array}{c|c} \mathrm{T}_{\pm}^{\perp,\perp} & \mathrm{T}_{\pm}^{\perp,\parallel} \\ \hline \mathrm{T}_{\pm}^{\parallel,\perp} & \mathrm{T}_{\pm}^{\parallel,\parallel} \end{array}\right), \quad \mathrm{K}_{\pm} = \left(\begin{array}{c|c} \mathrm{K}_{\pm}^{\perp,\perp} & \mathrm{K}_{\pm}^{\perp,\parallel} \\ \hline \mathrm{K}_{\pm}^{\parallel,\perp} & \mathrm{K}_{\pm}^{\parallel,\parallel} \end{array}\right) \tag{28}$$

$$\left(\mathrm{K}_{\pm}^{a\,b}\right)_{pq} = \left\langle \mathbf{j}_p^a \middle| \boldsymbol{\mathcal{K}}_{\pm} \middle| \mathbf{j}_q^b \right\rangle, \quad \left(\mathrm{T}_{\pm}^{a\,b}\right)_{pq} = \left\langle \mathbf{j}_p^a \middle| \boldsymbol{\mathcal{T}}_{\pm} \middle| \mathbf{j}_q^b \right\rangle \tag{29}$$

$$\mathrm{E}_0 = \left(\mathrm{E}_0^{\perp}|\mathrm{E}_0^{\parallel}\right)^{\mathsf{T}}, \quad \mathrm{H}_0 = \left(\mathrm{H}_0^{\perp}|\mathrm{H}_0^{\parallel}\right)^{\mathsf{T}} \tag{30}$$

and

$$\left(\mathrm{E}_0^a\right)_p = \left\langle \mathbf{j}_p^a, \mathbf{e}_0 \right\rangle \quad \left(\mathrm{H}_0^a\right)_p = \left\langle \mathbf{j}_p^a, \mathbf{h}_0 \right\rangle \tag{31}$$

with $a, b = \parallel, \perp$. The finite-dimensional system has $2(N^{\parallel} + N^{\perp})$ degrees of freedom.

We now decompose the Green's function as the sum of the static Green's function g_0, defined in (4), and a regular difference term $g_{d\pm}$

$$g_{\pm}(\mathbf{r}-\mathbf{r}') = g_0(\mathbf{r}-\mathbf{r}') + g_{d\pm}(\mathbf{r}-\mathbf{r}') \tag{32}$$

where

$$g_{d\pm}(\mathbf{r}-\mathbf{r}') = \frac{e^{-j\frac{k^{\pm}}{2}|\mathbf{r}-\mathbf{r}'|}}{4\pi\, j}k_{\pm}\mathrm{sinc}\left\{\frac{k^{\pm}}{2}\left|\mathbf{r}-\mathbf{r}'\right|\right\}. \tag{33}$$

In the past, the splitting of the Green's function into its static component and a difference term has been used to introduce well-conditioned and accurate scheme for the low-frequency analysis of PEC targets with the MFIE [58]. By applying this decomposition to the operators $\boldsymbol{\mathcal{T}}_{\pm}$ and $\boldsymbol{\mathcal{K}}_{\pm}$, defined in (21a) and (21b), we obtain

$$\begin{aligned} \boldsymbol{\mathcal{T}}_{\pm} &= +\frac{1}{jk^{\pm}}\boldsymbol{\mathcal{T}}_0^{\parallel} - jk^{\pm}\boldsymbol{\mathcal{T}}_0^{\perp} + \boldsymbol{\mathcal{T}}_{d\pm} \\ \boldsymbol{\mathcal{K}}_{\pm} &= \boldsymbol{\mathcal{K}}_0 + \boldsymbol{\mathcal{K}}_{d\pm} \end{aligned} \tag{34}$$

where $\boldsymbol{\mathcal{T}}_0^{\parallel}$ and $\boldsymbol{\mathcal{T}}_0^{\perp}$ are the static operators defined in (3) and (11), and

$$\boldsymbol{\mathcal{T}}_{d\pm}\{\mathbf{w}\}(\mathbf{r}) = jk^{\pm}\hat{\mathbf{n}} \times \hat{\mathbf{n}} \times \int_{\partial\Omega} g_{d\pm}(\mathbf{r}-\mathbf{r}')\mathbf{w}(\mathbf{r}')dS' + \frac{1}{jk^{\pm}}\hat{\mathbf{n}} \times \hat{\mathbf{n}} \times \int_{\partial\Omega} \nabla g_{d\pm}(\mathbf{r}-\mathbf{r}')\nabla'_S \cdot \mathbf{w}(\mathbf{r}')dS' \tag{35}$$

$$\boldsymbol{\mathcal{K}}_0\{\mathbf{w}\}(\mathbf{r}) = \hat{\mathbf{n}} \times \hat{\mathbf{n}} \times \int_{\partial\Omega} \mathbf{w}(\mathbf{r}') \times \nabla' g_0(\mathbf{r}-\mathbf{r}')dS' \tag{36}$$

$$\boldsymbol{\mathcal{K}}_{d\pm}\{\mathbf{w}\}(\mathbf{r}) = \hat{\mathbf{n}} \times \hat{\mathbf{n}} \times \int_{\partial\Omega} \mathbf{w}(\mathbf{r}') \times \nabla' g_{d\pm}(\mathbf{r}-\mathbf{r}')dS'. \tag{37}$$

The above decomposition considerably simplifies the calculation of the finite dimensional operators $\mathrm{T}_{\pm}^{a\,b}$ with $a, b = \parallel, \perp$, which are obtained by projecting the operator $\boldsymbol{\mathcal{T}}_{\pm}$ along the longitudinal and transverse static modes because $\{\mathbf{j}_k^{\parallel}\}$ and $\{\mathbf{j}_k^{\perp}\}$

diagonalize the static operators $\mathcal{T}_0^{\perp}$ and $\mathcal{T}_0^{\parallel}$

$$\left(\mathrm{T}_{\pm}^{\parallel\parallel}\right)_{pq} = \left\langle \mathbf{j}_p^{\parallel}, \mathcal{T}_{\pm}\mathbf{j}_q^{\parallel}\right\rangle = \frac{\gamma_p^{\parallel}}{jk^{\pm}}\delta_{p,q} - jk^{\pm}\left\langle \mathbf{j}_p^{\parallel}, \mathcal{T}_0^{\perp}\mathbf{j}_q^{\parallel}\right\rangle + \left\langle \mathbf{j}_p^{\parallel}, \mathcal{T}_{d\pm}\mathbf{j}_q^{\parallel}\right\rangle \quad (38a)$$

$$\left(\mathrm{T}_{\pm}^{\perp\parallel}\right)_{pq} = \left\langle \mathbf{j}_p^{\perp}, \mathcal{T}_{\pm}\mathbf{j}_q^{\parallel}\right\rangle \approx \left\langle \mathbf{j}_p^{\perp}, \mathcal{T}_{d\pm}\mathbf{j}_q^{\parallel}\right\rangle \quad (38b)$$

$$\left(\mathrm{T}_{\pm}^{\parallel\perp}\right)_{pq} = \left\langle \mathbf{j}_p^{\parallel}, \mathcal{T}_{\pm}\mathbf{j}_q^{\perp}\right\rangle \approx \left\langle \mathbf{j}_p^{\parallel}, \mathcal{T}_{d\pm}\mathbf{j}_q^{\perp}\right\rangle \quad (38c)$$

$$\left(\mathrm{T}_{\pm}^{\perp\perp}\right)_{pq} = \left\langle \mathbf{j}_p^{\perp}, \mathcal{T}_{\pm}\mathbf{j}_q^{\perp}\right\rangle = -jk^{\pm}\gamma_p^{\perp}\delta_{p,q} + \left\langle \mathbf{j}_p^{\perp}, \mathcal{T}_{d\pm}\mathbf{j}_q^{\perp}\right\rangle \quad (38d)$$

where $\delta_{p,q}$ is the Kronecker delta, and we have exploited the fact that $\langle \mathbf{j}_p^{\parallel}, \mathcal{T}_0^{\parallel}\mathbf{j}_q^{\perp}\rangle = \langle \mathbf{j}_p^{\perp}, \mathcal{T}_0^{\parallel}\mathbf{j}_q^{\parallel}\rangle = 0$, $\langle \mathbf{j}_p^{\perp}, \mathcal{T}_0^{\parallel}\mathbf{j}_q^{\perp}\rangle = 0$, $\langle \mathbf{j}_p^{\parallel}, \mathcal{T}_0^{\parallel}\mathbf{j}_q^{\parallel}\rangle = \gamma_p^{\parallel}\delta_{p,q}$, $\langle \mathbf{j}_p^{\perp}, \mathcal{T}_0^{\perp}\mathbf{j}_q^{\perp}\rangle = \gamma_p^{\perp}\delta_{p,q}$ and $\langle \mathbf{j}_p^{\parallel}, \mathcal{T}_0^{\perp}\mathbf{j}_q^{\perp}\rangle \approx \langle \mathbf{j}_p^{\perp}, \mathcal{T}_0^{\perp}\mathbf{j}_q^{\parallel}\rangle \approx 0$. The numerical computation of the terms $\langle \mathbf{j}_p^{a}, \mathcal{T}_{d\pm}\mathbf{j}_q^{b}\rangle$, with $a, b = \parallel, \perp$ is straightforward since their kernels are regular functions. These terms are the only ones depending on the operating frequency. The decomposition of Green's function into the sum of a static term and of a regular difference term relieves us from the task of computing almost all the integrals with (integrable) singularity, which usually results in longer computational time compared to their regular counterpart. There are however two exceptions: $\langle \mathbf{j}_p^{\parallel}, \mathcal{T}_0^{\perp}\mathbf{j}_q^{\parallel}\rangle$ and $\langle \mathbf{j}_p^{a}, \mathcal{K}_0^{\perp}\mathbf{j}_q^{b}\rangle$, with $a, b = \perp, \parallel$. These terms are frequency-independent, thus when the calculation of the scattering response of an object for multiple frequencies of the exciting field is required, they can be conveniently precalculated and stored away, while only the regular terms must be calculated at any frequencies.

B. Low-Frequency Analysis

Surface integral formulations may suffer from ill-conditioning due to low-frequency breakdown. The low-frequency breakdown phenomenon manifests when the operating wavelength is much larger than the dimension of the object [59], and originates from the different frequency-scaling of the terms associated with the vector and the scalar potentials. This is a common scenario that may be encountered in several applications, including metamaterials and electromagnetic bandgap (EBG) structures, or in the analysis of interconnects and packaging. This problem has been addressed by using quasi-Helmholtz decompositions, such as loop/star [54], [55], [59], loop-tree [13], [60], tree-cotree [10], or null-pinv [61] decompositions, followed by a basis rearrangement [62], [63]. It is also worth pointing out that some formulations are immune from this problem, such as the N-Müller formulation [64], or the formulation obtained by augmenting the traditional EFIE by including charge as extra unknown [65], [66].

In this section, we summarize the behavior of the PMCHWT at very low frequencies. In this limit, the frequency dependence of the elements of the matrix Z follows different scaling laws, which are easily determined by following [63], [67]:

$$\begin{pmatrix} \mathrm{T}_{\pm}^{\perp\perp} & \mathrm{T}_{\pm}^{\parallel\perp} \\ \mathrm{T}_{\pm}^{\perp\parallel} & \mathrm{T}_{\pm}^{\parallel\parallel} \end{pmatrix} \xrightarrow{\omega\downarrow 0} \begin{pmatrix} -jk^{\pm}\Gamma^{\perp} & j\left(k^{\pm}\right)^3\mathrm{T}_2^{\parallel\perp} \\ j\left(k^{\pm}\right)^3\mathrm{T}_2^{\perp\parallel} & +\Gamma^{\parallel}/jk^{\pm} \end{pmatrix} \quad (39)$$

$$\begin{pmatrix} \mathrm{K}_{\pm}^{\perp\perp} & \mathrm{K}_{\pm}^{\perp\parallel} \\ \mathrm{K}_{\pm}^{\parallel\perp} & \mathrm{K}_{\pm}^{\parallel\parallel} \end{pmatrix} \xrightarrow{\omega\downarrow 0} \begin{pmatrix} \left(k^{\pm}\right)^2\mathrm{K}_2^{\perp\perp} & \mathrm{K}_0^{\parallel\perp} \\ \mathrm{K}_0^{\perp\parallel} & \mathrm{K}_0^{\parallel\parallel} \end{pmatrix} \quad (40)$$

where $\Gamma^{\perp}$ and $\Gamma^{\parallel}$ are diagonal matrices, $\Gamma^{\perp} = \mathrm{diag}\{\gamma_1^{\perp}, \gamma_2^{\perp}, \ldots, \gamma_{N^{\perp}}^{\perp}\}$, $\Gamma^{\parallel} = \mathrm{diag}\{\gamma_1^{\parallel}, \gamma_2^{\parallel}, \ldots, \gamma_{N^{\parallel}}^{\parallel}\}$, and

$$T_2^{\parallel\perp} = \frac{1}{8\pi}\int_{\partial\Omega}\mathbf{j}_p^{\parallel}(\mathbf{r})\cdot\int_{\partial\Omega}\left|\mathbf{r}-\mathbf{r}'\right|\mathbf{j}_q^{\perp}(\mathbf{r}')dSdS' \quad (41)$$

$$K_2^{\perp\perp} = -\frac{1}{8\pi}\int_{\partial\Omega}\mathbf{j}_p^{\perp}(\mathbf{r})\cdot\int_{\partial\Omega}\frac{(\mathbf{r}-\mathbf{r}')}{|\mathbf{r}-\mathbf{r}'|}\times\mathbf{j}_q^{\perp}(\mathbf{r}')dSdS'. \quad (42)$$

Thus, by using (39) and (40) it easy to prove that, in the static limit, the discrete matrix Z approaches the matrix Z_0 which exhibits the following frequency dependence:

$$Z_0 = \begin{bmatrix} \mathcal{O}(\omega) & \mathcal{O}(\omega^3) & \mathcal{O}(\omega^2) & \mathcal{O}(1) \\ \mathcal{O}(\omega^3) & \mathcal{O}(\omega^{-1}) & \mathcal{O}(1) & \mathcal{O}(1) \\ \mathcal{O}(\omega^2) & \mathcal{O}(1) & \mathcal{O}(\omega) & \mathcal{O}(\omega^3) \\ \mathcal{O}(1) & \mathcal{O}(1) & \mathcal{O}(\omega^3) & \mathcal{O}(\omega^{-1}) \end{bmatrix}. \quad (43)$$

The excitation vector associated with a plane wave exhibits the following dependencies [63]:

$$\left[E_0^{\perp}, E_0^{\parallel}, H_0^{\perp}, H_0^{\parallel}\right]^{\mathsf{T}} = [\mathcal{O}(\omega), \mathcal{O}(1), \mathcal{O}(\omega), \mathcal{O}(1)]^{\mathsf{T}}. \quad (44)$$

Following [63], we introduce the rearrangement and scaling of the basis

$$\tilde{\mathrm{Z}} = \mathrm{D}_1\,\mathrm{Z}\,\mathrm{D}_2 \quad (45)$$

where $D_1 = \mathrm{diag}\{k_-^{-1}\mathrm{I}_{N^{\perp}}, \mathrm{I}_{N^{\parallel}}, k_-^{-1}\mathrm{I}_{N^{\perp}}, \mathrm{I}_{N^{\parallel}}\}$, $D_2 = \mathrm{diag}\{\mathrm{I}_{N^{\perp}}, i\,k_-\mathrm{I}_{N^{\parallel}}, \mathrm{I}_{N^{\perp}}, i\,k_-\mathrm{I}_{N^{\parallel}}\}$, $\mathrm{I}_{N^{\perp}}$ is the $N^{\perp}\times N^{\perp}$ identity matrix, and $\mathrm{I}_{N^{\parallel}}$ is the $N^{\parallel}\times N^{\parallel}$ identity matrix. After the above rearrangement the matrix $\tilde{\mathrm{Z}}$ is well-behaved.

IV. Results and Discussion

A. Sphere

We first consider the scattering from a sphere. This problem has an analytical solution [68], [69]. Fig. 1 shows the convergence of the numerical eigenvalues $\{\gamma_k^{\parallel}\}$ and $\{\gamma_k^{\perp}\}$ toward their analytical counterpart, given by (5) and (12), as a function of the triangular mesh density. From this point forward, we will consider the static basis calculated using a triangular mesh with $N_p = 1000$ nodes and $N_t = 1996$ triangles. The first eight longitudinal modes are shown in Fig. 2, the first eight transverse modes are shown in Fig. 3.

In the discrete problem, the orthogonality between any pair of longitudinal modes and between any pair of transverse modes is always guaranteed, because the matrices $\mathrm{T}^{\circlearrowleft\circlearrowleft}$ and $\mathrm{T}^{\star\star}$ are real and symmetric. This property is indeed verified at the numerical level with machine precision. Although we expect the mutual product between a transverse and a longitudinal static mode to be nearly zero, this is only approximately the case because the sub-domain basis functions used to represent the longitudinal modes, namely the "star" functions, are not rigorously curl-free [55]. Thus, it is clarifying to calculate the

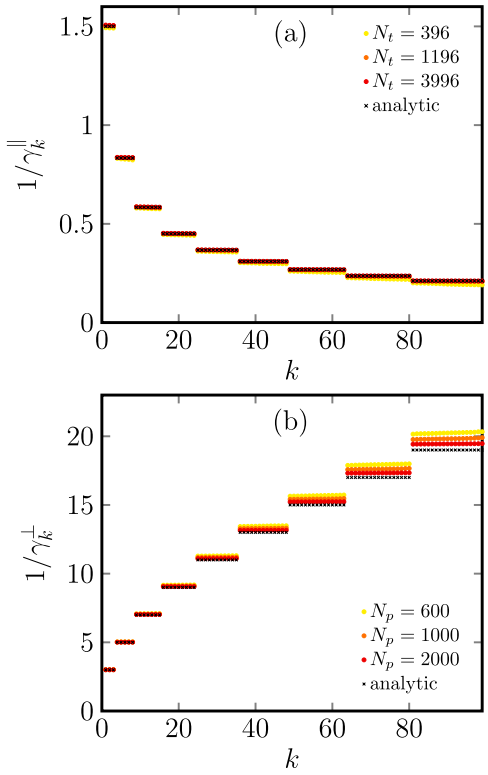

Fig. 1. Reciprocals of the first 100 eigenvalues (a) $\gamma_k^{\parallel}$ and (b) $\gamma_k^{\perp}$ associated with the longitudinal and transverse static modes of the unit radius sphere. The eigenvalues were computed for several densities of the triangular surface mesh (filled circles of different colors) having N_t elements and N_p nodes and then compared to their respective analytical values.

"mutual" Gram matrix G, whose occurrences are defined as $g_{hk} = \langle \mathbf{j}_h^{\perp}, \mathbf{j}_k^{\parallel} \rangle$. The maximum occurrence of the mutual Gram matrix is 0.024 for a sphere with the considered surface mesh, assuming $\|\mathbf{j}_h^{\parallel}\| = \|\mathbf{j}_h^{\perp}\| = 1$, $\forall h$.

1) Gold Sphere: We initiate our discussion with the scattering problem from a gold sphere of radius $R = 100$ nm operating within the visible and near-infrared spectral range. We describe the gold permittivity by interpolating experimental data [70]. At these frequencies, a metal nano-object may undergo plasmonic resonances, which have an electrostatic origin [29]. The sphere is excited by a linearly polarized plane wave of wavelength λ.

The scattering efficiency, defined as the scattering cross section normalized by the geometrical cross section G (which is $G = \pi R^2$ [69] in this case) is plotted in Fig. 4 as a function of λ. We compare the results of different solutions that were obtained by incrementally increasing the number of modes employed in the expansion (23) while keeping $N^{\parallel} = N^{\perp}$. The reference Mie solution [69] is included for reference. For $N^{\parallel} = N^{\perp} = 5$, the numerical solution is in good agreement with the reference solution only in the long-wavelength regime, while it slightly deviates as λ approaches R. Increasing the number of modes to $N^{\parallel} = N^{\perp} = 10$ delivers good agreement over the entire investigated spectrum. In this latter case, the inversion of a 40×40 matrix is required at each frequency.

In Fig. 5, we show the condition number of the PMCHWT problem with and without the rearrangement of the basis described in Section III-B as a function of the sphere radius R, at $\lambda = 620$ nm. It is apparent that, without the basis rearrangement, the condition number exponentially increases, which is symptomatic of the low-frequency breakdown problem. By rearranging the basis, the condition number is constant over the whole investigated range of radii R.

We now present a more comprehensive error analysis. In particular, we define the relative error in the scattering efficiency as

$$\epsilon[\sigma_{sca}] = \left|\sigma_{sca} - \tilde{\sigma}_{sca}\right| / \tilde{\sigma}_{sca} \tag{46}$$

where $\tilde{\sigma}_{sca}$ is the reference solution obtained by solving the PMCHWT problem applying the boundary element method with $N^{\circlearrowleft} = 999$ loop functions and $N^{\star} = 1995$ star functions, associated with the same mesh used for the calculation of static modes. In Fig. 6(a), we plot $\epsilon[\sigma_{sca}]$ as a function of the wavelength λ, where the number of static modes is varied keeping $N^{\parallel} = N^{\perp}$. We note that for $N^{\parallel} = N^{\perp} \geq 10$ the achieved error is lower than 0.02 all over the investigated spectral range. The error only slowly decreases if the number of modes $N^{\parallel} = N^{\perp}$ is increased from 15 to 25.

We proceed to investigate the error in the evaluation of the equivalent surface currents, which are directly related to the total electric field on the object's surface. The relative error is defined as

$$\epsilon[\mathrm{J}] = \left\|\mathrm{J} - \tilde{\mathrm{J}}\right\|_2 / \left\|\tilde{\mathrm{J}}\right\|_2 \tag{47}$$

where $\tilde{\mathrm{J}}$ is the reference loop/star solution and $\|\cdot\|_2$ is the Euclidean norm. In Fig. 6(b), we show $\epsilon[\mathrm{J}]$ as a function of λ. It's evident that achieving a prescribed error necessitates more static basis functions than Fig. 6(a).

In a subsequent test, we assess the convergence of the static modes solution with a near-field excitation source. Here, an electric point dipole excites a gold sphere of radius $R = 100$ nm. The dipole is placed 30 nm away from the sphere's surface and oriented as shown in the inset of Fig. 7. We evaluate the total scattered power W_{sca} using an increasing number of longitudinal/transverse static modes ($N^{\parallel} = N^{\perp} = 5, 10, 15$) and compared it with the reference Mie solution. As soon as $N^{\parallel} = N^{\perp} = 15$, the two solutions become indistinguishable.

In Fig. 8, we investigate the two relative errors $\epsilon[W_{sca}]$ and $\epsilon[\mathbf{j}]$, with the loop/star solution as a reference. Fig. 8(a) shows that the total scattered power evaluated using the static modes rapidly converges toward the loop/star solution. However, the convergence of the surface currents, shown in Fig. 8(b), is considerably slower due to the rapid spatial variations of the surface current near the exciting dipole. These variations necessitate higher-order static modes for accurate description.

2) High-Permittivity Sphere: We now consider a high permittivity sphere, assumed to be nondispersive in time with relative permittivity $\varepsilon_R = 16$. Sub-wavelength objects of sufficiently high permittivity may support scattering resonances, which have a magnetostatic origin [31], [34].

In Fig. 9, we calculate the scattering efficiency σ_{sca} as a function of the wavelength λ of the exciting, linearly polarized, plane wave. We consider different solutions computed using an increasing number of static modes, maintaining $N^{\parallel} = N^{\perp}$. The

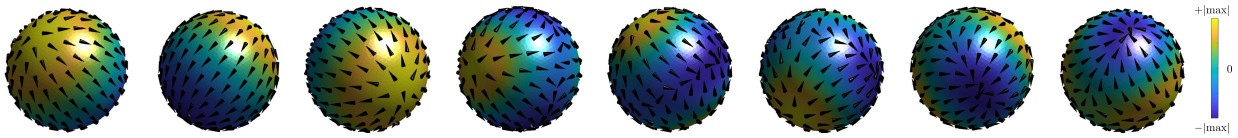

Fig. 2. Longitudinal static modes of a sphere, displayed in ascending order according to their static eigenvalue. The first eight modes are presented: the initial three correspond to $n = 1$ (electric dipole) and the subsequent five to $n = 2$ (electric quadrupole). The arrows indicate the direction of the surface current density field, while the varying colors denote the surface charge density.

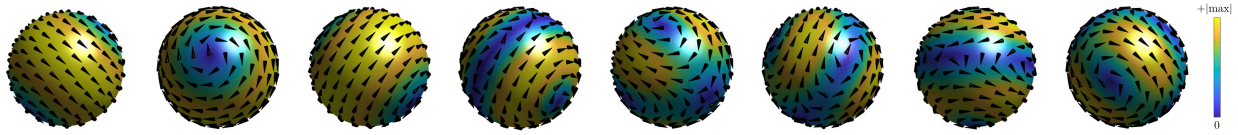

Fig. 3. Transverse static modes of a sphere, displayed in ascending order according to their static eigenvalue. The first eight modes are presented: the initial three correspond to $n = 1$ (magnetic dipole) and the subsequent five to $n = 2$ (magnetic quadrupole). The arrows indicate the direction of the surface current density field, the colors denote the magnitude of the current density field.

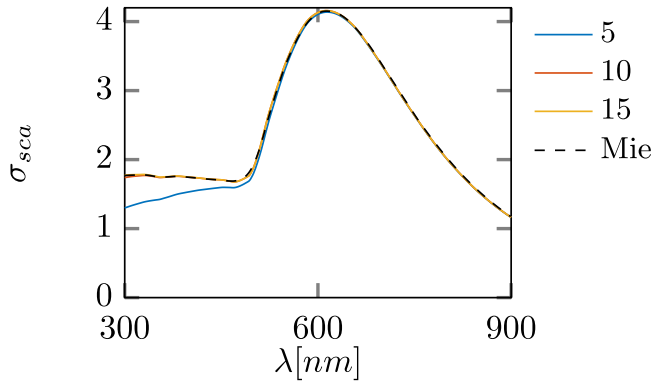

Fig. 4. Scattering efficiency σ_{sca} of a gold sphere with radius $R = 100$ nm under the excitation of a linearly polarized plane wave at wavelength λ. σ_{sca} is calculated using the PMCHWT with an incrementing number of longitudinal and transverse static modes ($N^{\parallel} = N^{\perp} = 5, 10, 15$). The reference Mie solution is also provided for comparison, and is shown by the black dashed line.

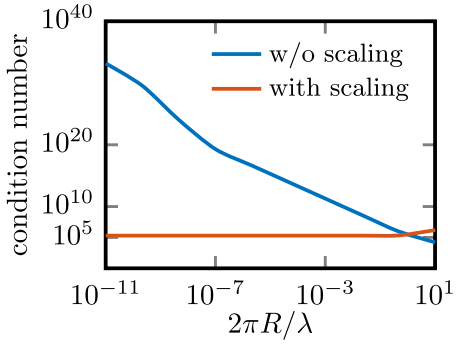

Fig. 5. Comparison of the condition number with and without basis rearrangement and scaling, as a function of the size parameter $2\pi R/\lambda$, under the assumption of $N^{\parallel} = N^{\perp} = 15$. The study involves a gold sphere of varying radius R, excited by a linearly polarized plane wave at wavelength $\lambda = 620$ nm.

analytic Mie solution [68], [69], shown with a black dashed line, serves as our reference.

While the solution displays a good match with the Mie solution at lower frequencies when $N^{\parallel} = N^{\perp} = 5$, the accuracy of the solution deteriorates at higher frequencies and fails to describe some peaks of the scattering response. However, elevating the number of modes utilized to $N^{\parallel} =$

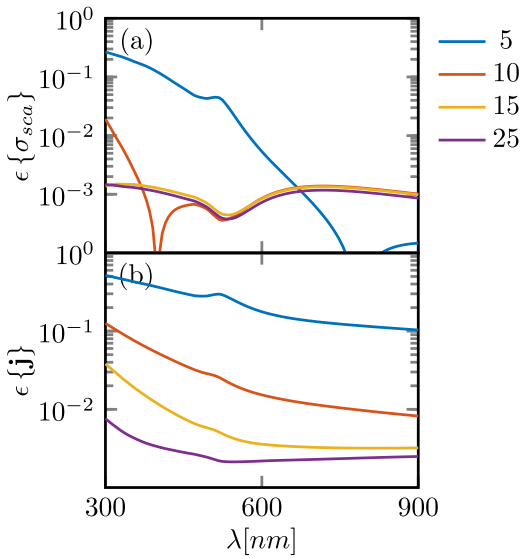

Fig. 6. Error made in the evaluation of (a) scattering efficiency $\epsilon[\sigma_{sca}]$ and (b) equivalent surface currents $\epsilon[\mathbf{j}]$ of a gold sphere $R = 100$ nm by using $N^{\parallel} = N^{\perp} = 5, 10, 15, 25$ static modes corresponding to 20, 40, 60, 100 degrees of freedom. The reference solutions use the loop/star method with 999 loop and 1996 star functions, totaling 5998 degrees of freedom. In both cases, a PMCHWT formulation is used. The sphere is excited by a linearly polarized plane wave as a function of the wavelength λ.

$N^{\perp} = 15$ leads to a remarkable agreement throughout the entire examined spectrum.

We now quantify the errors in the scattering efficiency and in the surface currents of the static mode solution. Fig. 10(a) presents $\epsilon[\sigma_{sca}]$ as a function of λ, employing an increasing number of modes, ensuring $N^{\perp} = N^{\parallel}$. With $N^{\perp} = N^{\parallel} = 5$, the error remains within an acceptable range provided λ significantly exceeds the object's dimensions. However, the error sharply rises for wavelengths below 600 nm. Adopting $N^{\perp} = N^{\parallel} = 25$ results in a low error all over the investigated spectrum. The error only slightly exceeds 0.01 at the resonances. A further increase in the number of basis functions improves the convergence, particularly in the vicinity of the resonance peaks. In Fig. 10(b), we show $\epsilon[\mathrm{J}]$ as a function of λ. Compared to panel (a), the relative error is higher. To verify the convergence of the static mode expansion, we also tested

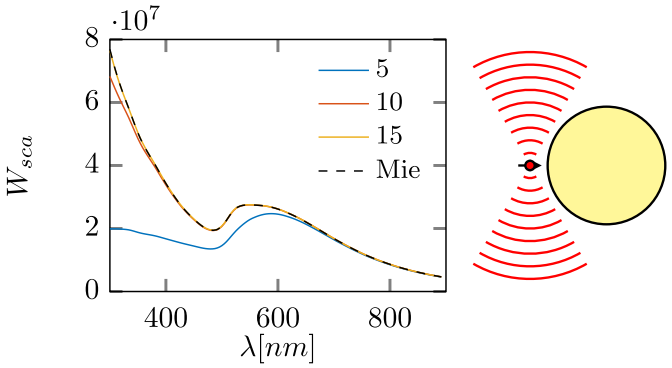

Fig. 7. Plot of the power W_{sca} scattered by a gold sphere with radius $R = 100$ nm, which is excited by an electric point dipole. The dipole is located at a distance of 30 nm from the surface of the particle, and oriented as shown in the inset. W_{sca} is evaluated as a function of the wavelength λ using the PMCHWT with an increasing number of longitudinal/transverse static modes ($N^{\parallel} = N^{\perp} = 5, 10, 15$). For comparison, The reference Mie solution is also shown with a black dashed line.

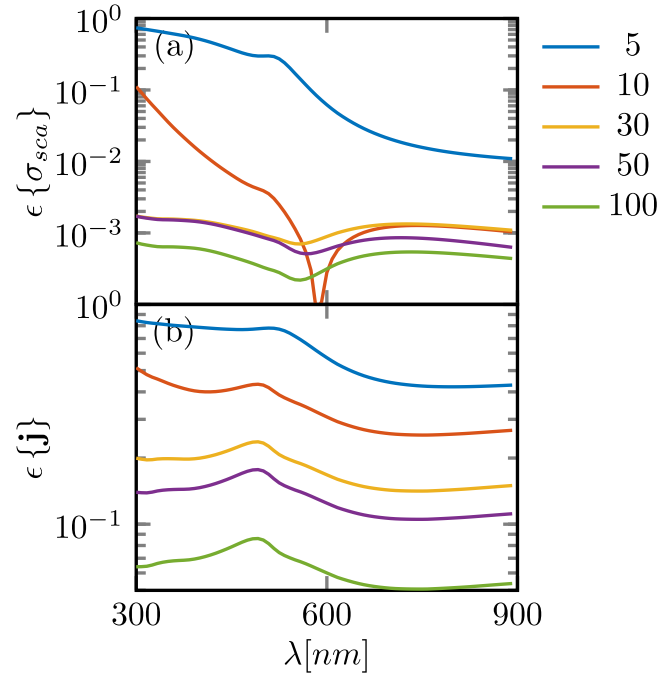

Fig. 8. Error made in the evaluation of (a) scattered power W_{sca} and (b) equivalent surface currents $\epsilon[\mathbf{j}]$ of a gold sphere $R = 100$ nm by solving the PMCHWT using $N^{\parallel} = N^{\perp} = 5, 10, 30, 50, 100$ static modes. The reference values were obtained by solving the PMCHWT using 999 loop and 1996 star functions. The sphere is excited by a dipole, located at a distance of 30 nm from the surface of the particle and oriented as shown in the inset of Fig. 7.

with $N^{\perp} = N^{\parallel} = 500$, leading to numerical errors less than 0.009 for the σ_{sca} and less than 0.03 for $\mathbf{j}$ across the entire investigated spectral range.

B. Rod

We now consider a noncanonical shape, namely a 3-D rod. We model this shape as a superellipsoid, whose boundary has the implicit equation $(x/a)^r + (y/b)^r + (z/a)^r = 1$, with $b = 0.5a$, $c = 0.25a$, and $r = 6$. We used the public domain code developed by Per-Olof Persson and Gilbert Strang [71] to generate a surface mesh with 1000 nodes and 1996 triangular elements. The first eight longitudinal and eight transverse static modes are shown in Figs. 11 and 12, respectively.

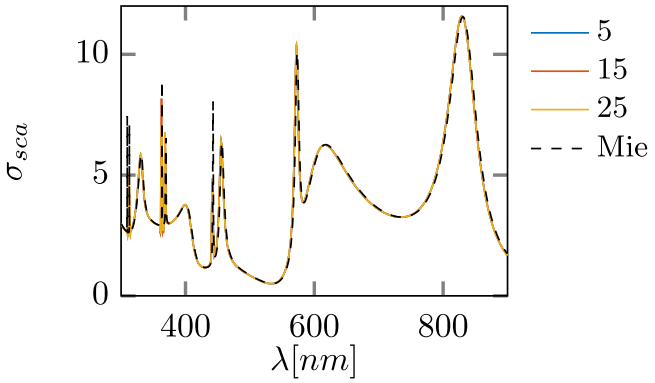

Fig. 9. Scattering efficiency σ_{sca} of a dielectric sphere with $R = 100$ nm and $\varepsilon_R = 16$, excited by a linearly polarized plane wave at wavelength λ. The evaluation is performed using the PMCHWT with an increasing number of longitudinal and transverse static modes ($N^{\parallel} = N^{\perp} = 5, 15, 25$). The reference Mie solution is also shown for comparison (black dashed line).

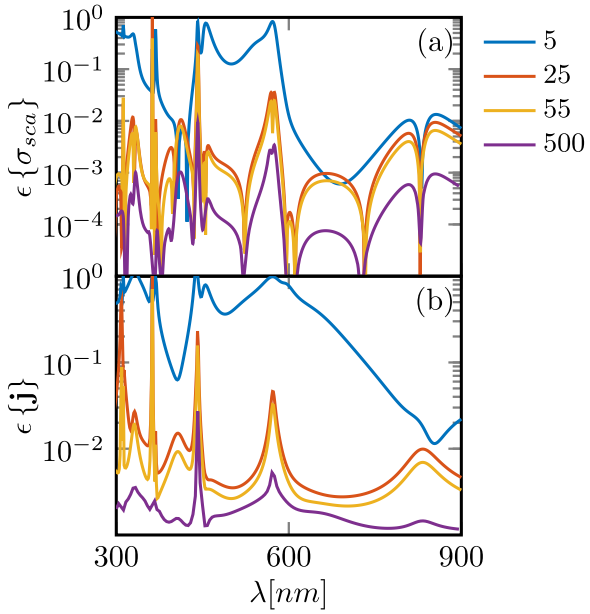

Fig. 10. Error made in the evaluation of (a) scattering efficiency σ_{sca} and (b) equivalent surface currents $\mathbf{j}$ of a dielectric sphere with $\varepsilon_R = 16$ and $R = 100$ nm. The evaluation is performed using the PMCHWT equation with the static mode basis assuming $N^{\parallel} = N^{\perp} = 5, 25, 55, 500$. The reference values are obtained by solving the PMCHWT and using the loop/star expansion. The sphere is excited by a linearly polarized plane wave as a function of the wavelength λ.

1) Gold Rod: First, we investigate a gold [70] rod with $a = 100$ nm, excited by a plane wave linearly polarized along the direction $(\hat{\mathbf{x}} + \hat{\mathbf{y}})/\sqrt{2}$ and propagating along the $\hat{\mathbf{z}}$ axis. In Fig. 13, we plot the spectrum of the scattering efficiency σ_{sca}, obtained by increasing the number of modes $N^{\perp} = N^{\parallel} = 5, 10, 15$. We take as reference the loop/star solution, with 5984 total degrees of freedom. Only five longitudinal and transverse modes (20 total degrees of freedom) are sufficient to achieve a sufficiently good agreement with the reference solution over the whole investigated spectrum, demonstrating a drastic reduction of the total number of unknowns.

In Fig. 14, we carry out a more systematic analysis of the error on the scattering cross section $\epsilon[\sigma_{sca}]$ (a), and on the equivalent surface currents $\epsilon[\mathbf{j}]$ (b). In comparison to the sphere case, these errors appear to be slightly higher. However, similar to our previous numerical experiments, we can

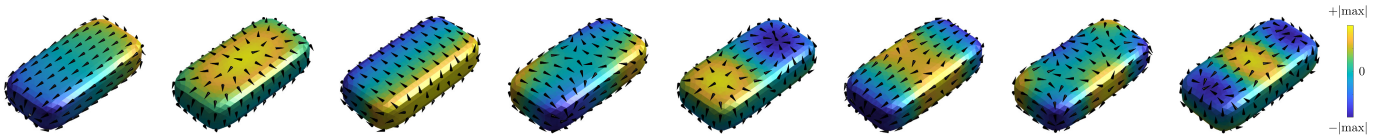

Fig. 11. First eight longitudinal static modes of a rod with semi-axis 1:0.5:0.25. Modes are presented in ascending lexicographic order, sorted according to their respective static eigenvalues. The arrows represent the direction of the surface current density field, the colors represent the surface charge density.

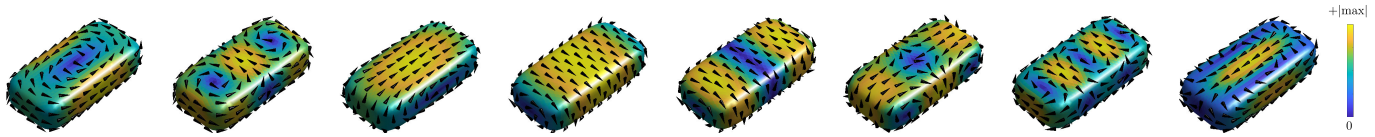

Fig. 12. First eight transverse static modes of a rod with semi-axis 1:0.5:0.25. Modes are presented in ascending lexicographic order, sorted according to their respective static eigenvalues. The arrows represent the direction of the surface current density field, the colors represent the magnitude of the current density field.

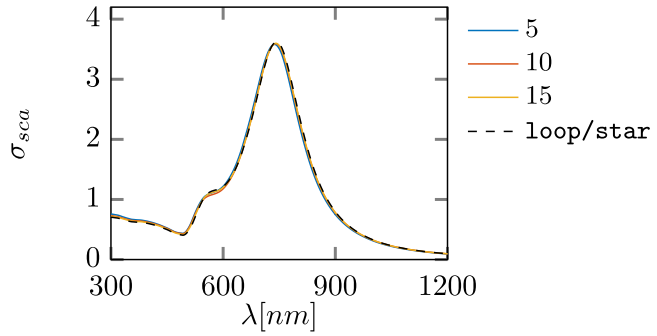

Fig. 13. Scattering efficiency σ_{sca} of a gold rod with semi-axis $a = 100$ nm, $b = 0.5a$, and $c = 0.25a$ evaluated with an increasing number of longitudinal and transverse static modes $N^{\parallel} = N^{\perp} = 5, 15, 25, 35, 55$. The rod is excited by a linearly polarized plane wave. The reference loop/star solution (black dashed line) is also shown for comparison.

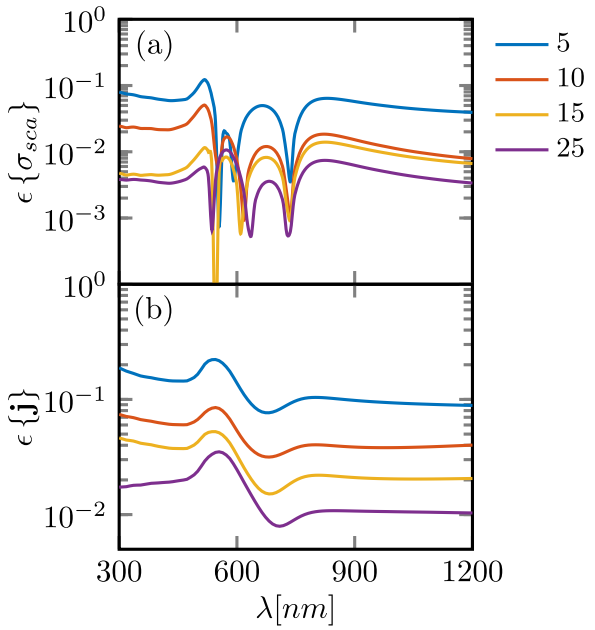

Fig. 14. Error ϵ in the evaluation of (a) scattering efficiency σ_{sca} and of (b) equivalent surface current density of a gold rod with semi-axis $a = 100$ nm, $b = 0.5a$, and $c = 0.25a$ by solving the PMCHWT using the static mode basis with $N^{\parallel} = N^{\perp} = 5, 15, 20, 25$. Reference values are derived from the PMCHWT solution using loop/star expansion.

conclude that: 1) the errors associated with the surface currents are an order of magnitude higher than the errors related to scattering efficiency and 2) the rate of convergence is not uniform as a function of the number of employed modes and it slows down as $N^{\parallel} = N^{\perp}$ increases.

2) High-Permittivity Rod: Next, we examine a high-permittivity rod, assuming a constant relative permittivity over the investigated frequency spectrum, with a value of $\varepsilon_R = 16$. The scattering efficiency spectrum (σ_{sca}) is presented in Fig. 15, where it's calculated using an increasing number of static modes. We use as reference the loop/star solution, with a total of 5984 degrees of freedom. If the wavelength is much larger than the dimension of the rod, $N^{\perp} = N^{\parallel} = 15$ suffices to accurately describe the scattering cross section. However, the precision deteriorates when the wavelength is comparable to the rod's linear dimensions, especially near high-frequency resonance peaks. Only by increasing the number of modes $N^{\perp} = N^{\parallel}$ to 55, all the resonance peaks, including the high-frequency ones, are correctly described.

Fig. 16 offers a more quantitative analysis of the errors (a) $\epsilon[\sigma_{sca}]$ and (b) $\epsilon[\mathbf{j}]$. We observe that, for larger wavelength an error below $\epsilon[\sigma_{sca}] < 0.01$ and $\epsilon[\mathbf{j}] < 0.2$, can be achieved with $N^{\perp} = N^{\parallel} = 25$ modes. However, when the wavelength becomes comparable to the rod's largest dimension, as many as 55 longitudinal and transverse static modes are necessary to contain the error. Even then, the precision deteriorates near the resonance peaks. To verify the convergence of the static mode

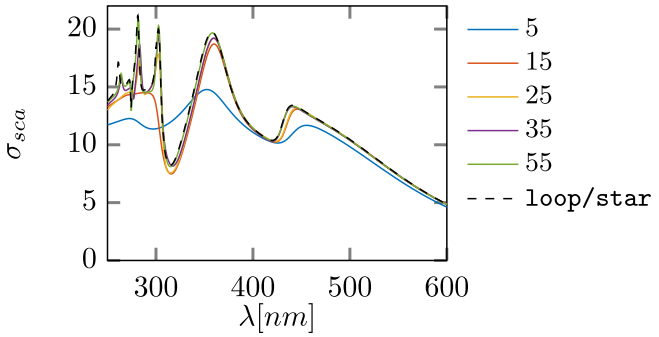

Fig. 15. Scattering efficiency σ_{sca} of a dielectric rod with $\varepsilon_R = 16$ and semi-axis $a = 100$ nm, $b = 0.5a$, and $c = 0.25a$. The evaluation is performed for an increasing number of longitudinal and transverse static modes $N^{\parallel} = N^{\perp} = 5, 15, 25, 35, 55$. The rod is excited by a linearly polarized plane wave. The reference loop/star solution (black dashed line) is also shown for comparison.

expansion, we also tested with $N^{\perp} = N^{\parallel} = 500$. We obtained errors less than 0.0015 for σ_{sca} and less than 0.0068 for $\mathbf{j}$ across the entire investigated spectral range.

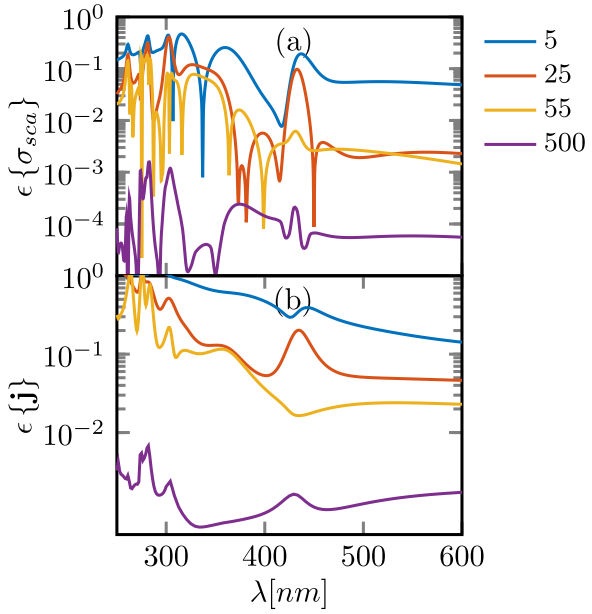

Fig. 16. Error ϵ in the evaluation of (a) scattering efficiency σ_{sca} and of (b) equivalent surface current density of a dielectric rod with $\varepsilon_R = 16$ with semi-axis $a = 100$ nm, $b = 0.5a$, and $c = 0.25a$ by solving the PMCHWT using an increasing number of longitudinal and transverse static modes $N^{\parallel} = N^{\perp} = 5, 25, 55, 500$. The reference values are obtained by solving the PMCHWT using the loop/star expansion.

To conclude, while a higher number of modes is needed to accurately describe the unknown current densities compared to previous scenarios, the required count remains significantly lower than the number of loop/star functions needed to achieve comparable accuracy.

C. Solution of Multiple Scattering Problems

The use of static mode basis may be particularly convenient for numerically solving multiple scattering problems from arrays of objects of the same shape but varying in size and orientation. In this section, we examine finite-size periodic arrays of n particles, composed of spheres and triangular prisms. In both cases, the particles are placed at the nodes of a $\sqrt{n} \times \sqrt{n}$ square grid of pitch 250 nm. These arrays are excited by a plane wave linearly polarized in the plane of the array, and propagating in the direction orthogonal to the array's plane with a wavelength $\lambda = 600$ nm.

Table I displays the errors made in the evaluation of the scattering efficiency and of the surface currents via the static mode solution of electromagnetic scattering from several arrays of spheres. We assume the loop/star solution as a reference. The arrays consist of $n = 1, 4, 9, 16, 25$ spherical particles of radius $R = 100$ nm, and are excited by a plane-wave linear polarization along an array's axis. The single sphere's surface mesh has 200 nodes and 396 triangles, which corresponds to a maximum edge length of the mesh's triangles $\approx\lambda/17$. A loop/star description results in $1188\,n$ unknowns. We instead utilized $N^{\parallel} = 10$ longitudinal and $N^{\perp} = 10$ transverse modes to describe the electric and magnetic surface currents on each nanoparticle, leading to $40\,n$ unknowns. The errors achieved consistently remain below 4% for both the scattering efficiency and the currents.

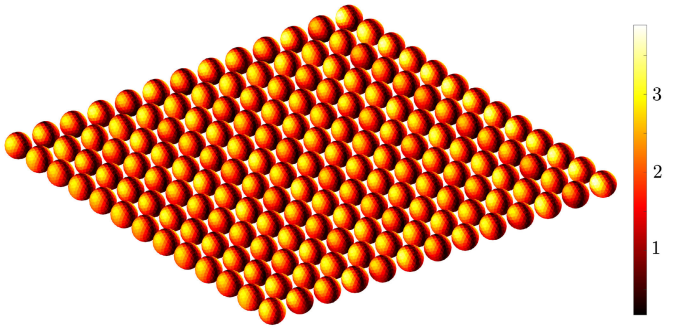

Fig. 17. Magnitude of the electric field on the particles' surface of a finite-size 13×13 periodic array of 169 gold spheres with radius $R = 100$ nm and edge-edge distance 50 nm. The edge of the array is 3.2 μm. The array is excited by a linearly polarized plane of wavelength $\lambda = 600$ nm, with unit intensity. The solution has been computed by using the static mode expansion with $N^{\parallel} = N^{\perp} = 10$.

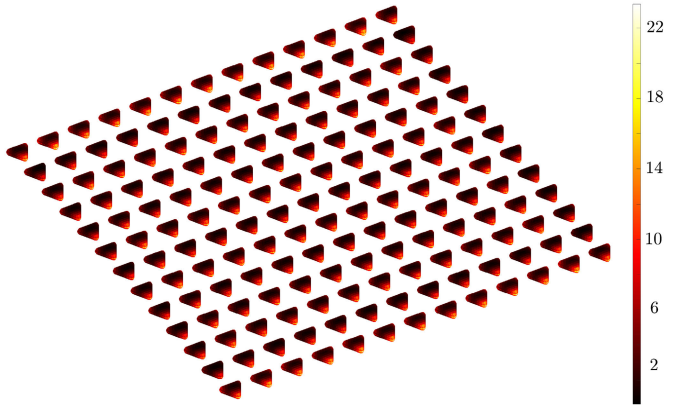

Fig. 18. Magnitude of the electric field on the particles' surface of a finite-size 13×13 periodic array of 169 gold triangular prisms with base edge 170 nm, basis height 153 nm, thickness 50 nm, and center-center distance 250 nm. The edge of the array is 3.2 μm. The array is excited by a plane wave of wavelength $\lambda = 600$ nm, linearly polarized in the arrays' plane along the basis height, with unit intensity. The solution has been computed by using the static mode expansion with $N^{\parallel} = N^{\perp} = 10$.

TABLE I
ERRORS IN THE SOLUTION OF THE SCATTERING PROBLEM BY A PERIODIC ARRAY MADE BY n SPHERES

n	1	4	9	16	25
$\epsilon[\sigma_{sca}][\%]$	0.2	0.68	2.5	2.8	3.3
$\epsilon[\mathbf{j}_{sca}]$	2.0	3.3	3.4	3.5	3.4

In Fig. 17, we show the magnitude of the electric field on the particles' surface of a 13×13 finite size array calculated using the static mode expansion.

In addition, in Fig. 18, we show the magnitude of the electric field on the particles' surface of a 13×13 array made of equilateral triangular prisms with a base edge of 170 nm, a height of 153 nm, and a thickness of 50 nm. The plane wave exhibits linear polarization along the height of the base of the triangles, with unit intensity. The individual prism is characterized by a surface mesh with 182 nodes and 360 triangles. We considered $N^{\parallel} = 10$ longitudinal and $N^{\perp} = 10$ transverse modes to describe the electric and magnetic surface currents on each nanoparticle, achieving a reduced count of 6760 unknowns.

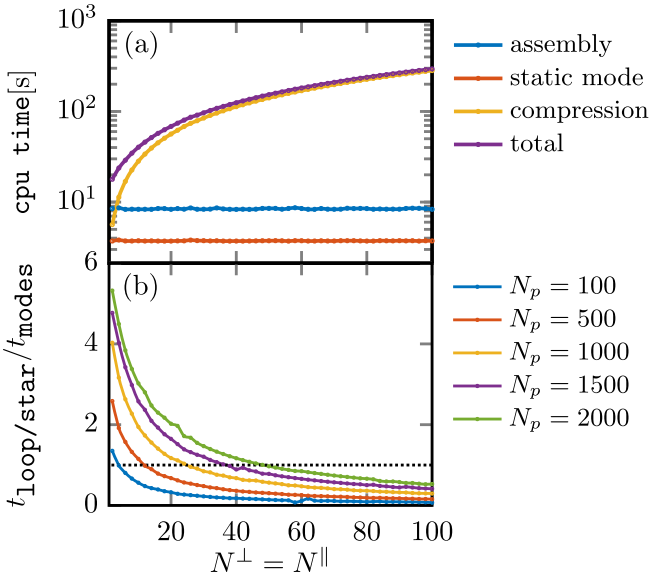

Fig. 19. (a) CPU-time (in seconds) of the different stages of the numerical solution of the scattering problem from a gold sphere with $R = 100$ nm excited by linearly polarized plane wave with $\lambda = 620$ nm as a function of the number of modes $N^\perp = N^\parallel$, for a given mesh $N_p = 500$, $N_t = 996$. (b) Ratio between the total CPU-time for the computation of the PMCHWT solution using the loop/star basis $t_{loop/star}$ and using the static mode basis t_{modes}. This ratio is evaluated as a function of the number of static modes $N^\perp = N^\parallel$ for different meshes with different number of nodes N_p.

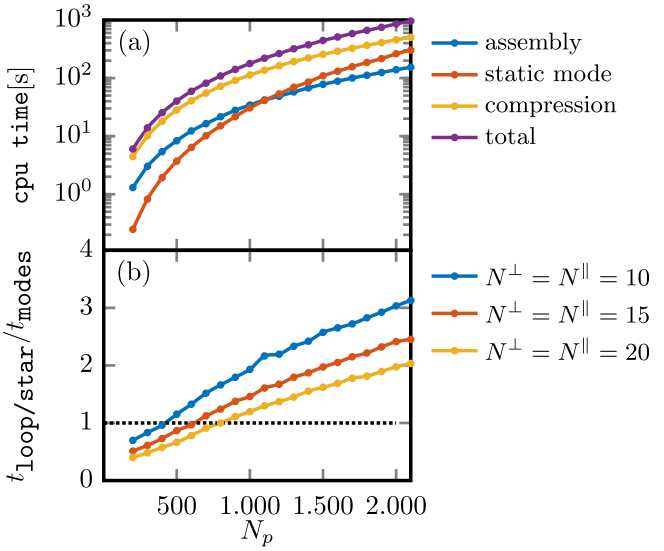

Fig. 20. (a) CPU-time (in seconds) of the different stages of the numerical solution of the scattering problem from a gold sphere with $R = 100$ nm excited by linearly polarized plane wave with $\lambda = 620$ nm, as a function of the mesh density (number of number of nodes N_p), for a prescribed number of static modes $N^\perp = N^\parallel = 10$. (b) Ratio between the total CPU-time for the computation of the PMCHWT solution using the loop/star basis $t_{loop/star}$ and using the static mode basis t_{modes}. This ratio is evaluated as a function of the mesh density, for different number of static modes.

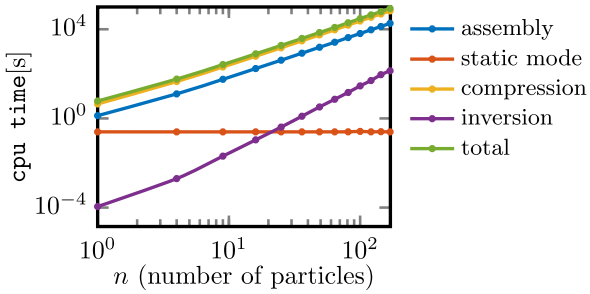

Fig. 21. CPU-time (in seconds) of the different stages of the numerical solution of the scattering problem from a square array of n spheres (radius 100 nm, edge-edge distance 250 nm): assembly of the matrices using the loop/star basis; generation of the longitudinal/transverse static modes; compression, by passing from loop/star to static modes; direct inversion (LU); total time. The code is implemented in FORTRAN, and run on a single CPU.

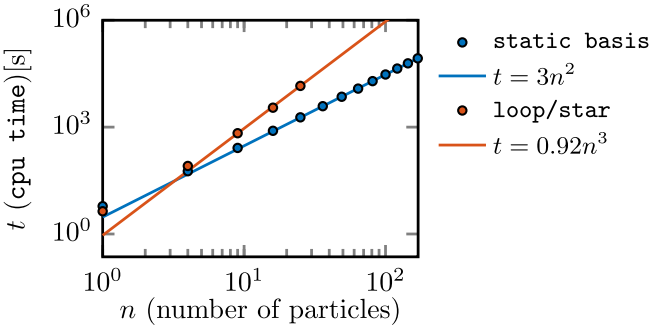

Fig. 22. Total execution CPU-time (in seconds) of the numerical solution of the scattering problem from an array of n spheres by using loop/star basis functions and by using the static modes basis. Both codes are implemented in FORTRAN and run on a single CPU. The two fitting curves are shown with a continuous line. The same sphere's mesh ($N_p = 200$, $N_t = 396$) is used both for calculating the static modes and for the loop/star solution.

V. Computational Costs

The execution of our numerical algorithm consists of four distinct stages: 1) the "assembly" stage, during which the matrices $T_\pm$, $K_\pm$ and of the vectors E_0, H_0 are constructed in the loop/star basis; 2) the "static mode generation" stage, where the longitudinal/transverse static modes of an isolated object are computed by solving the eigenvalue problems (15) and (16); 3) the "compression" stage, which involves transforming matrices $T_\pm$, $K_\pm$ from a loop/star representation into a static modes representation; and 4) the "inversion" stage, during which direct inversion of the compressed matrices is performed using LU decomposition. In the following, we provide a time-analysis of the various phases of the numerical algorithm for two test cases: an isolated sphere, and an array of spheres. The FORTRAN code used for this analysis operates on a single CPU (Intel Xeon-Gold 6140 M 2.3 GHz).

A. Isolated Sphere

Fig. 19(a) illustrates the CPU-time (in seconds) taken by each stage of the numerical solution for the scattering problem from the isolated gold sphere of Section IV-A1. This is measured against the number of longitudinal and transverse static modes $N^\parallel = N^\perp$, for a predetermined mesh ($N_p = 500$, $N_t = 996$). Within the examined range ($N^\parallel = N^\perp = 1, \ldots, 100$) the time taken for the "inversion" and the "static mode generation" stages remains always negligible if compared with the "assembly" and "compression" stages. The compression stage typically demands the most time, increasing linearly with the number of transverse/longitudinal modes used.

Fig. 19(b) shows the ratio of CPU-time needed for the PMCHWT solution using the loop/star basis ($t_{\texttt{loop/star}}$) to that needed for a solution using $N^\perp = N^\parallel$ static modes ($t_{\texttt{modes}}$). This analysis was repeated across various mesh densities, which are defined by the number of nodes N_p.

The same mesh was used to calculate both the static modes and the loop/star solution.

Fig. 20(a) presents the CPU-time (in seconds) of the different stages of the numerical solution of the scattering problem, but this time as a function of the *mesh density*, i.e., the number of nodes N_p, with a prescribed number of modes $N^{\parallel} = N^{\perp} = 10$. Within the investigated range ($N_p \leq 2100$), the time taken for the matrix inversion using LU decomposition remains negligible compared to the time required for the assembly of the matrices $\mathrm{K}_{\pm}$ and $\mathrm{T}_{\pm}$ and for their compression. Both assembly and compression times are proportional to N_p^2. Compression is still typically the most time-consuming stage, although for very dense meshes, the time spent for static mode calculation becomes comparable, as it is proportional to N_p^3.

Fig. 20(b) displays the ratio of $t_{\texttt{loop/star}}$ to $t_{\texttt{modes}}$ as a function of the mesh density. This analysis was repeated for different numbers of modes. The same mesh was used for calculating the static modes and the loop/star solution. We found that the static mode solution is advantageous, i.e., $t_{\texttt{loop/star}} > t_{\texttt{modes}}$, only for sufficiently dense meshes.

B. Particles' Array

In Fig. 21, we show the CPU-time (in seconds) of the different stages of the PMCHWT solution of the electromagnetic scattering problem a finite-size periodic array of spheres, as a function of the number n of spheres ($n = 1, 4, 9, 16, \ldots, 169$). The geometry and mesh are identical to those detailed in Section IV-C. We represent the electric and magnetic surface currents on each nanoparticle using $N^{\parallel} = 10$ longitudinal and $N^{\perp} = 10$ transverse modes, thus $40\,n$ unknowns.

In the investigated range ($n \leq 169$), the total computational time is always dominated by the compression time, which scales as $\propto n^2$. The assembly time, which also scales as $\propto n^2$, contributes significantly to the total execution time. The time required for the computation of the static modes of the isolated sphere, which are used as basis, is negligible and it does not depend on the array's size. The inversion time, which scales as $\propto n^3$, is negligible compared with the compression time if, as in our case, the dimensions of the arrays do not surpass a given number of particles (n_{th}). The value of n_{th} can be estimated by extrapolating the curves in Fig. 21, and it is $n_{th} \approx 80\,000$ particles.

Fig. 22 compares the total CPU-time required for the PMCHWT solution using the static modes basis with the corresponding time required for the loop/star solution, as a function of n. The same sphere's mesh ($N_p = 200$, $N_t = 396$) is used both for calculating the static modes and for the loop/star solution. For $n > 4$, the static mode solution proves more advantageous, with the speed-up further increasing as n increases.

To deduce the scaling laws, we fit the total computational time of the PMCHWT solution in terms of the static basis using the curve $t = 3n^2$, and in terms of the loop/star solution using the curve $t = 0.92n^3$. The ratio is $0.3\ n$. Consequently, for a 5×5 array, the CPU-time required for the loop/star solution is 7.5 times greater than the time required for the static mode solution. For $n = 169$, we extrapolate that the static mode solution is $50\times$ faster. However, this could not be empirically verified as the time estimated for the loop/star solution computation was prohibitively long.

VI. Conclusion

In this article, we introduced a set of "static" surface current modes and used them to expand the unknown surface current densities in the surface integral equations governing the electromagnetic scattering problem from penetrable objects. We demonstrated the efficacy of the static mode expansion in the PMCHWT formulation [21], [42], [43]. We found several characteristics that make the use of static modes appealing.

1) The retarded Green's function, constituting the kernel of integral operators recurring in surface integral formulations such as the PMCHWT, may be decomposed as the sum of the static Green's function (with integrable singularity) and a proper difference (which is a regular function). The resulting integral operators containing the static Green's function are diagonalized by the static modes, regularizing the overall problem [72].
2) The use of the static mode expansion, when combined with an appropriate rescaling and rearranging of the unknowns, makes the PMCHWT formulation immune from the low-frequency breakdown problem.
3) The static modes only depend on the shape of the object, making them universally applicable across varying operating frequencies and material properties of the object. This facilitates a unified, frequency-independent description of any scattering scenario involving objects of a given shape, outperforming other basis sets (like characteristic modes) that depend on frequency and materials.

As test cases, we considered the scattering from both metal and high-permittivity dielectric objects. We found that for objects of size smaller than the wavelength of operation, only a few modes are sufficient to accurately describe the emergent scattering response. The static mode expansion, thus, significantly cuts down the unknowns compared to loop/star or Rao-Wilton-Glisson function discretization, without compromising solution accuracy.

The most time-consuming stage of the PMCHWT numerical solution using static modes and direct inversion is typically the "compression" stage, which is the change of the basis used to represent the impedance matrix from the loop/star set to the static modes set. In the scattering problem from an isolated particle, the use of the static modes set is convenient in terms of total CPU-time, compared with the PMCHWT numerical solution using loop/star set and direct inversion, only when few static modes are needed to describe the surface currents. In contrast, the advantages of static modes are more pronounced in multiple scattering problems from particle arrays of n objects with similar shapes but differing orientations and sizes. Even for small arrays, the static modes solution is faster than the loop/star solution with direct inversion, with this lead increasing linearly with particle count n.

Notwithstanding, for scattering problems involving object arrays, optimal CPU-time performance is usually achieved

through fast factorization schemes, iterative solvers, and effective preconditioning [4]. Nevertheless, the compression of the matrix equations by static modes can be advantageous in several scenarios. For instance, when calculating the scattering from a specified particle array under numerous excitation conditions—a scenario where iterative solvers fall short, as the iterations need to be started anew for each right-hand side [37]. In addition, since implementing fast factorization schemes may be expensive in terms of human cost, static mode compression allows baseline implementations of the method of moments without fast factorization to address problems that would not be possible otherwise.

REFERENCES

[1] R. E. Collin, *Antennas and Radiowave Propagation*. New York, NY, USA: McGraw-Hill, 1985.

[2] N. Yu and F. Capasso, "Flat optics with designer metasurfaces," *Nature Mater.*, vol. 13, no. 2, pp. 139–150, Feb. 2014. [Online]. Available: https://www.nature.com/articles/nmat3839

[3] M. Khorasaninejad et al., "Achromatic metasurface lens at telecommunication wavelengths," *Nano Lett.*, vol. 15, no. 8, pp. 5358–5362, Aug. 2015, doi: 10.1021/acs.nanolett.5b01727.

[4] W. C. Chew, J.-M. Jin, E. Michielssen, and J. Song, *Fast and Efficient Algorithms in Computational Electromagnetics*. Boston, MA, USA: Artech House, Jul. 2000.

[5] O. M. Bucci and G. D. Massa, "Use of characteristic modes in multiple-scattering problems," *J. Phys. D, Appl. Phys.*, vol. 28, no. 11, pp. 2235–2244, Nov. 1995. [Online]. Available: https://iopscience.iop.org/article/10.1088/0022-3727/28/11/003/meta

[6] G. Angiulli, G. Amendola, and G. Di Massa, "Characteristic modes in multiple scattering by conducting cylinders of arbitrary shape," *Electromagnetics*, vol. 18, no. 6, pp. 593–612, Nov. 1998, doi: 10.1080/02726349808908615.

[7] A. Doicu, T. Wriedt, and Y. A. Eremin, *Light Scattering by Systems of Particles: Null-Field Method With Discrete Sources: Theory and Programs* (Springer Series in Optical Sciences). Berlin, Germany: Springer, 2006. [Online]. Available: https://www.springer.com/gp/book/9783540336969

[8] S. M. Rao, D. R. Wilton, and A. W. Glisson, "Electromagnetic scattering by surfaces of arbitrary shape," *IEEE Trans. Antennas Propagat.*, vol. AP-30, no. 3, pp. 409–418, May 1982.

[9] A. Bossavit, *Computational Electromagnetism: Variational Formulations, Complementarity, Edge Elements*. New York, NY, USA: Academic, 1998.

[10] R. Albanese and G. Rubinacci, "Integral formulation for 3D eddy-current computation using edge elements," *Proc. Inst. Elect. Eng.-Phys. Sci., Meas. Instrum., Manage. Educ.*, vol. 135, no. 7, pp. 457–462, Sep. 1988.

[11] G. Rubinacci and A. Tamburrino, "A broadband volume integral formulation based on edge-elements for full-wave analysis of lossy interconnects," *IEEE Trans. Antennas Propag.*, vol. 54, no. 10, pp. 2977–2989, Oct. 2006.

[12] D. Wilton, J. Lim, and S. Rao, "A novel technique to calculate the electromagnetic scattering by surfaces of arbitrary shape," in *Proc. URSI Radio Sci. Meeting*, 1993, p. 322.

[13] W.-L. Wu, A. W. Glisson, and D. Kajfez, "A study of two numerical solution procedures for the electric field integral equation at low frequency," *Appl. Comput. Electromagn. Soc. J.*, vol. 10, no. 3, pp. 69–80, Nov. 1995.

[14] L. Trintinalia and H. Ling, "First order triangular patch basis functions for electromagnetic scattering analysis," *J. Electromagn. Waves Appl.*, vol. 15, no. 11, pp. 1521–1537, Jan. 2001.

[15] A. Buffa and S. Christiansen, "A dual finite element complex on the barycentric refinement," *Math. Comput.*, vol. 76, no. 260, pp. 1743–1769, May 2007. [Online]. Available: https://www.jstor.org/stable/40234460

[16] R. D. Graglia, D. R. Wilton, and A. F. Peterson, "Higher order interpolatory vector bases for computational electromagnetics," *IEEE Trans. Antennas Propag.*, vol. 45, no. 3, pp. 329–342, Mar. 1997.

[17] F. Vico, L. Greengard, and Z. Gimbutas, "Boundary integral equation analysis on the sphere," *Numerische Math.*, vol. 128, no. 3, pp. 463–487, Nov. 2014, doi: 10.1007/s00211-014-0619-z.

[18] A. Ayala, X. Claeys, P. Escapil-Inchauspé, and C. Jerez-Hanckes, "Local multiple traces formulation for electromagnetics: Stability and preconditioning for smooth geometries," *J. Comput. Appl. Math.*, vol. 413, Oct. 2022, Art. no. 114356. [Online]. Available: https://www.sciencedirect.com/science/article/pii/S0377042722001583

[19] L.-W. Li, X.-K. Kang, and M.-S. Leong, *Spheroidal Wave Functions in Electromagnetic Theory*. Hoboken, NJ, USA: Wiley, Apr. 2004.

[20] R. J. Garbacz, "Modal expansions for resonance scattering phenomena," *Proc. IEEE*, vol. 53, no. 8, pp. 856–864, Apr. 1965.

[21] Y. Chang and R. Harrington, "A surface formulation for characteristic modes of material bodies," *IEEE Trans. Antennas Propag.*, vol. AP-25, no. 6, pp. 789–795, Nov. 1977.

[22] R. Harrington, J. Mautz, and Y. Chang, "Characteristic modes for dielectric and magnetic bodies," *IEEE Trans. Antennas Propag.*, vol. AP-20, no. 2, pp. 194–198, Mar. 1972.

[23] Y. Chen and C.-F. Wang, *Characteristic Modes: Theory and Applications in Antenna Engineering*. Hoboken, NJ, USA: Wiley, Jun. 2015.

[24] M. Faenzi et al., "Metasurface antennas: New models, applications and realizations," *Sci. Rep.*, vol. 9, no. 1, p. 10178, Jul. 2019. [Online]. Available: https://www.nature.com/articles/s41598-019-46522-z

[25] J. Van Bladel, "A discussion of Helmholtz theorem on a surface," *Int. J. Electron. Commun.*, vol. 47, no. 3, pp. 131–136, 1993. [Online]. Available: http://hdl.handle.net/1854/LU-202008

[26] J.-C. Nedelec, *Acoustic and Electromagnetic Equations: Integral Representations for Harmonic Problems* (Applied Mathematical Sciences). New York, NY, USA: Springer-Verlag, 2001. [Online]. Available: https://www.springer.com/gp/book/9780387951553

[27] A. Buffa and R. Hiptmair, "Galerkin boundary element methods for electromagnetic scattering," in *Topics in Computational Wave Propagation: Direct and Inverse Problems* (Lecture Notes in Computational Science and Engineering), M. Ainsworth, P. Davies, D. Duncan, B. Rynne, and P. Martin, Eds. Berlin, Heidelberg: Springer, 2003, pp. 83–124.

[28] C. Forestiere, G. Gravina, G. Miano, M. Pascale, and R. Tricarico, "Electromagnetic modes and resonances of two-dimensional bodies," *Phys. Rev. B, Condens. Matter*, vol. 99, no. 15, Apr. 2019, Art. no. 155423, doi: 10.1103/PhysRevB.99.155423.

[29] I. D. Mayergoyz, D. R. Fredkin, and Z. Zhang, "Electrostatic (plasmon) resonances in nanoparticles," *Phys. Rev. B, Condens. Matter*, vol. 72, no. 15, Oct. 2005, Art. no. 155412, doi: 10.1103/PhysRevB.72.155412.

[30] G. Miano, G. Rubinacci, and A. Tamburrino, "Numerical modeling for the analysis of plasmon oscillations in metallic nanoparticles," *IEEE Trans. Antennas Propag.*, vol. 58, no. 9, pp. 2920–2933, Sep. 2010.

[31] C. Forestiere et al., "Magnetoquasistatic resonances of small dielectric objects," *Phys. Rev. Res.*, vol. 2, no. 1, Feb. 2020, Art. no. 013158, doi: 10.1103/PhysRevResearch.2.013158.

[32] C. Forestiere, G. Miano, M. Pascale, and R. Tricarico, "Quantum theory of radiative decay rate and frequency shift of surface plasmon modes," *Phys. Rev. A, Gen. Phys.*, vol. 102, no. 4, Oct. 2020, Art. no. 043704, doi: 10.1103/PhysRevA.102.043704.

[33] C. Forestiere and G. Miano, "Operative approach to quantum electrodynamics in dispersive dielectric objects based on a polarization-mode expansion," *Phys. Rev. A, Gen. Phys.*, vol. 106, no. 3, Sep. 2022, Art. no. 033701, doi: 10.1103/PhysRevA.106.033701.

[34] C. Forestiere, G. Miano, and G. Rubinacci, "Resonance frequency and radiative Q-factor of plasmonic and dielectric modes of small objects," *Phys. Rev. Res.*, vol. 2, no. 4, Nov. 2020, Art. no. 043176, doi: 10.1103/PhysRevResearch.2.043176.

[35] C. Forestiere and G. Miano, "Time-domain formulation of electromagnetic scattering based on a polarization-mode expansion and the principle of least action," *Phys. Rev. A, Gen. Phys.*, vol. 104, no. 1, Jul. 2021, Art. no. 013512, doi: 10.1103/PhysRevA.104.013512.

[36] E. Suter and J. R. Mosig, "A subdomain multilevel approach for the efficient MoM analysis of large planar antennas," *Microw. Opt. Technol. Lett.*, vol. 26, no. 4, pp. 270–277, 2000.

[37] V. V. S. Prakash and R. Mittra, "Characteristic basis function method: A new technique for efficient solution of method of moments matrix equations," *Microw. Opt. Technol. Lett.*, vol. 36, no. 2, pp. 95–100, Jan. 2003, doi: 10.1002/mop.10685.

[38] L. Matekovits, V. A. Laza, and G. Vecchi, "Analysis of large complex structures with the synthetic-functions approach," *IEEE Trans. Antennas Propag.*, vol. 55, no. 9, pp. 2509–2521, Sep. 2007.

[39] A. Freni, P. De Vita, P. Pirinoli, L. Matekovits, and G. Vecchi, "Fast-factorization acceleration of MoM compressive domain-decomposition," *IEEE Trans. Antennas Propag.*, vol. 59, no. 12, pp. 4588–4599, Dec. 2011.

[40] G. Vecchi, L. Matekovits, P. Pirinoli, and M. Orefice, "Hybrid spectral-spatial method for the analysis of printed antennas," *Radio Sci.*, vol. 31, no. 5, pp. 1263–1270, Sep. 1996.

[41] G. Vecchi, L. Matekovits, P. Pirinoli, and M. Orefice, "A numerical regularization of the EFIE for three-dimensional planar structures in layered media," *Int. J. Microw. Millim.-Wave Comput.-Aided Eng.*, vol. 7, no. 6, pp. 410–431, 1997.

[42] T. Wu and L. L. Tsai, "Scattering from arbitrarily-shaped lossy dielectric bodies of revolution," *Radio Sci.*, vol. 12, no. 5, pp. 709–718, Sep. 1977.

[43] A. J. Poggio and E. K. Miller, "Integral equation solutions of three-dimensional scattering problems," in *Computer Techniques for Electromagnetics* (International Series of Monographs in Electrical Engineering), R. Mittra, Ed. New York, NY, USA: Pergamon, Jan. 1973, pp. 159–264. [Online]. Available: https://www.sciencedirect.com/science/article/pii/B9780080168883500088

[44] R. F. Harrington, *Field Computation by Moment Methods*. Hoboken, NJ, USA: Wiley, 1993.

[45] R. F. Harrington, "Boundary integral formulations for homogeneous material bodies," *J. Electromagn. Waves Appl.*, vol. 3, no. 1, pp. 1–15, Jan. 1989.

[46] R. Hiptmair and C. Jerez-Hanckes, "Multiple traces boundary integral formulation for Helmholtz transmission problems," *Adv. Comput. Math.*, vol. 37, no. 1, pp. 39–91, Jul. 2012, doi: 10.1007/s10444-011-9194-3.

[47] X. Claeys and R. Hiptmair, "Electromagnetic scattering at composite objects : A novel multi-trace boundary integral formulation," *ESAIM: Math. Model. Numer. Anal.*, vol. 46, no. 6, pp. 1421–1445, Nov. 2012. [Online]. Available: http://www.esaim-m2an.org/10.1051/m2an/2012011

[48] Z. Peng, K. Lim, and J. Lee, "Computations of electromagnetic wave scattering from penetrable composite targets using a surface integral equation method with multiple traces," *IEEE Trans. Antennas Propag.*, vol. 61, no. 1, pp. 256–270, Jan. 2013.

[49] C. Jerez-Hanckes, J. Pinto, and S. Tournier, "Local multiple traces formulation for high-frequency scattering problems," *J. Comput. Appl. Math.*, vol. 289, pp. 306–321, Dec. 2015. [Online]. Available: https://www.sciencedirect.com/science/article/pii/S0377042715000102

[50] R. Zhao, J. Hu, H. Zhao, M. Jiang, and Z. Nie, "Fast solution of electromagnetic scattering from homogeneous dielectric objects with multiple-traces EF/MFIE method," *IEEE Antennas Wireless Propag. Lett.*, vol. 16, pp. 2211–2215, 2017.

[51] P. Monk, *Finite Element Methods for Maxwell's Equations*. Oxford, U.K.: Clarendon Press, Apr. 2003.

[52] N. V. Nair and B. Shanker, "Generalized method of moments: A novel discretization technique for integral equations," *IEEE Trans. Antennas Propag.*, vol. 59, no. 6, pp. 2280–2293, Jun. 2011.

[53] A. Tamburrino, G. Piscitelli, and Z. Zhou, "The monotonicity principle for magnetic induction tomography," *Inverse Problems*, vol. 37, no. 9, Aug. 2021, Art. no. 095003, doi: 10.1088/1361-6420/ac156c.

[54] M. Burton and S. Kashyap, "A study of a recent, moment-method algorithm that is accurate to very low frequencies," *ACES J.*, vol. 10, no. 3, pp. 58–68, Nov. 1995.

[55] G. Vecchi, "Loop-star decomposition of basis functions in the discretization of the EFIE," *IEEE Trans. Antennas Propag.*, vol. 47, no. 2, pp. 339–346, Feb. 1999.

[56] H. Golub and C. F. V. Loan, *Matrix Computations*. Baltimore, MD, USA: Johns Hopkins Univ. Press, 1983.

[57] R. D. Graglia, "On the numerical integration of the linear shape functions times the 3-D green's function or its gradient on a plane triangle," *IEEE Trans. Antennas Propag.*, vol. 41, no. 10, pp. 1448–1455, Oct. 1993.

[58] E. Ubeda and J. M. Rius, "Divergence-conforming discretization of second-kind integral equations for the RCS computation in the Rayleigh frequency region," *Radio Sci.*, vol. 46, no. 5, pp. 1–10, Oct. 2011.

[59] D. R. Wilton and A. W. Glisson, "On improving the electric field integral equation at low frequencies," in *Proc. URSI Radio Sci. Meeting Dig.*, Los Angeles, CA, USA, Jun. 1981, pp. 22–24.

[60] F. P. Andriulli, "Loop-star and loop-tree decompositions: Analysis and efficient algorithms," *IEEE Trans. Antennas Propag.*, vol. 60, no. 5, pp. 2347–2356, May 2012.

[61] G. Miano and F. Villone, "A surface integral formulation of Maxwell equations for topologically complex conducting domains," *IEEE Trans. Antennas Propag.*, vol. 53, no. 12, pp. 4001–4014, Dec. 2005.

[62] J.-S. Zhao and W. Cho Chew, "Integral equation solution of Maxwell's equations from zero frequency to microwave frequencies," *IEEE Trans. Antennas Propag.*, vol. 48, no. 10, pp. 1635–1645, Oct. 2000.

[63] S. Y. Chen, W. Cho Chew, J. M. Song, and J.-S. Zhao, "Analysis of low frequency scattering from penetrable scatterers," *IEEE Trans. Geosci. Remote Sens.*, vol. 39, no. 4, pp. 726–735, Apr. 2001.

[64] P. Ylä-Oijala, H. Wallén, D. C. Tzarouchis, and A. Sihvola, "Surface integral equation-based characteristic mode formulation for penetrable bodies," *IEEE Trans. Antennas Propag.*, vol. 66, no. 7, pp. 3532–3539, Jul. 2018.

[65] M. Taskinen and P. Yla-Oijala, "Current and charge integral equation formulation," *IEEE Trans. Antennas Propag.*, vol. 54, no. 1, pp. 58–67, Jan. 2006.

[66] Z. G. Qian and W. C. Chew, "An augmented electric field integral equation for high-speed interconnect analysis," *Microw. Opt. Technol. Lett.*, vol. 50, no. 10, pp. 2658–2662, Oct. 2008, doi: 10.1002/mop.23736.

[67] C. Forestiere, G. Miano, G. Rubinacci, A. Tamburrino, L. Udpa, and S. Ventre, "A frequency stable volume integral equation method for anisotropic scatterers," *IEEE Trans. Antennas Propag.*, vol. 65, no. 3, pp. 1224–1235, Mar. 2017.

[68] G. Mie, "Beiträge zur optik trüber medien, speziell kolloidaler Metallösungen," *Annalen Physik*, vol. 330, no. 3, pp. 377–445, 1908, doi: 10.1002/andp.19083300302.

[69] C. F. Bohren and D. R. Huffman, *Absorption and Scattering of Light by Small Particles*. Hoboken, NJ, USA: Wiley, 2008.

[70] P. B. Johnson and R. W. Christy, "Optical constants of the noble metals," *Phys. Rev. B, Condens. Matter*, vol. 6, no. 12, pp. 4370–4379, Dec. 1972.

[71] P.-O. Persson and G. Strang, "A simple mesh generator in MATLAB," *SIAM Rev.*, vol. 46, no. 2, pp. 329–345, Jan. 2004. [Online]. Available: https://www.jstor.org/stable/20453511

[72] A. I. Nosich, "The method of analytical regularization in wave-scattering and eigenvalue problems: Foundations and review of solutions," *IEEE Antennas Propag. Mag.*, vol. 41, no. 3, pp. 34–49, Jun. 1999.

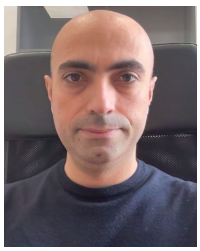

Carlo Forestiere (Member, IEEE) received the B.Sc., M.Sc. (summa cum laude), and Ph.D. degrees in electrical engineering from the University of Naples Federico II, Naples, Italy, in 2005, 2007, and 2010, respectively.

He is an Associate Professor with the University of Naples Federico II. From 2011 to 2014, he was a Post-Doctoral Research Fellow at the Boston University, Boston. He has authored or coauthored more than 60 scientific contributions in peer-reviewed journal articles and book chapters and has given over 20 invited talks and seminars. His research interests embrace applied electromagnetism and quantum technologies, and currently focus on nanophotonics, electromagnetic scattering, and computational electromagnetics.

Giovanni Gravina graduated (Hons.) in electronic engineering and Ph.D. degree in information technology and electrical engineering-34th Cycle from the University of Naples Federico II, Naples, Italy, in 2018 and 2022, respectively.

He is a Captain in the Italian Air Force. He entered the Air Force Academy in 2013. He was qualified as a Production Test Technician, since 2019, he has been working at the 10th Aircraft Maintenance Department (Galatina), where he mainly deals with ground and flight checks and technical management of the AM Training Fleets.

Giovanni Miano received the Laurea (summa cum laude) and Ph.D. degrees in electrical engineering from the University of Naples Federico II, Naples, Italy, in 1983 and 1989, respectively.

From 1984 to 1985, he was with the PS Division, CERN, Geneva, Switzerland. From 1989, he is the Full Professor at the Faculty of Engineering, University of Naples Federico II. In 1996, he was a Visiting Scientist at the GSI Laboratories, Darmstadt, Germany. In 1999, he was a Visiting Professor in the Department of Electrical Engineering, University of Maryland, College Park, ML, USA. From 2005 to 2009, he was the Director of the Dipartimento di Ingegneria Elettrical. He is the author or coauthor of more than 100 papers published in international journals, 100 papers published in international conference proceedings, two items in the Wiley Encyclopedia of Electrical and Electronic Engineering (New York: Wiley, 1999), and the monograph Transmission Lines and Lumped Circuits (New York: Academic, 2001). His current research interests include ferromagnetic materials, nonlinear dielectrics, plasmas, electrodynamics of continuum media, nanotechnology, and modeling of lumped and distributed circuits.

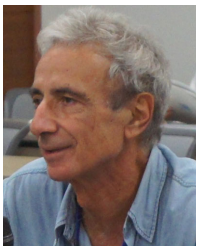

Guglielmo Rubinacci graduated in electronic engineering from the Università di Napoli, Naples, Italy, in 1975.

He is a Retired Professor of fundamentals in electrical engineering at the University of Napoli Federico II. From 1990 to 2022, he was a Full Professor and a Research affiliate at the MIT in 2015 to 2017. He was the Dean of the Faculty of Engineering at the University of Cassino from 1996 to 2003. As a Fulbright-Hays Fellow he was a Visiting Scientist at MIT in 1980 to 1981. His research interests are mainly in computational electromagnetics with applications in several fields such as plasma engineering in tokamaks and electromagnetic nondestructive evaluation.

Prof. Rubinacci was a member of the GEV09 sub-committee of the National Agency for the Evaluation of Universities and Research Institutes in 2012 to 2013 and 2015 to 2016. He received the Applied Electromagnetics and Mechanics Award for excellence in Applied Electromagnetics and Mechanics in 2009. He was the Chairman of the International Steering Committee of the COMPUMAG International Conference on the Computation of Electromagnetic Fields from 1990 to 1991 and acted as a scientific coordinator of several European and national research projects.

Antonello Tamburrino (Senior Member, IEEE) received the Laurea degree (summa cum laude) in electronic engineering from the University of Naples Federico II, Naples, Italy, in 1992, and the Ph.D. degree in electronic engineering from the Polytechnic of Turin, Turin, Italy, in 1996.

Since 2006, he has been a Full Professor of Electrical Engineering at the Department of Electrical and Information Engineering, University of Cassino and Southern Latium, Cassino, Italy. From 2014 to 2018, he was Full Professor of Electrical Engineering at the College of Engineering, Michigan State University, East Lansing, MI, USA. He has authored or co-authored more than 250 papers that have appeared in refereed international journals, books, and proceedings of international conferences, and he is Co-Editor of three proceedings. His current research interests include inverse problems, electromagnetic imaging, nondestructive evaluation, computational electromagnetism, plasmonics, and homogenization methods.

Dr. Tamburrino is currently an Editor-in-Chief for the scientific journal *International Journal on Applied Electromagnetics and Mechanics*, Subject Editor for the scientific journal NDT & E International, an Associate Editor for scientific *journal Nondestructive Testing and Evaluation* and Chair of the scientific committee of the Italian Association for Nondestructive Testing, Monitoring, Diagnostic.

Open Access funding provided by 'Università degli Studi di Napoli "Federico II"' within the CRUI CARE Agreement